ACS APPLIED NANO MATERIALS

www.acsanm.org Article

Shallow Impurity States in Doped Silicon Substrates Enabling High Responsivity for Graphene Mid-Infrared Photodetectors

Vinh X. Ho, Yifei Wang, Leslie Howe, Michael P. Cooney, and Nguyen Q. Vinh*

Cite This: *ACS Appl. Nano Mater.* 2022, 5, 12477−12486 Read Online

ACCESS | Metrics & More | Article Recommendations | Supporting Information

ABSTRACT: The practical realization of optoelectronic devices operating in the mid-infrared region is stimulated by both fundamental interests and applications ranging from spectroscopy, sensing, imaging, and security to communications. Despite significant achievements in semiconductors, essential barriers including the cryogenic operation and complicated growth processes prevent the applications of mid-infrared detectors. Graphene is widely used in modern electronics, but its low absorption limits photodetection. It is therefore of interest to extend the performance of graphene photodetectors into the mid-infrared region. Here, we first demonstrate pure graphene photodetectors operating in a broadband range from the deep ultraviolet to the mid-infrared region by utilizing photoionization of shallow impurities and over band gap excitation in highly doped Si:B and Si:P substrates. We have observed a photoresponsivity of ∼5 A/W under the mid-infrared illumination at room temperature. This approach paves the way for a concept of dual-photogating effect induced by both highly doped Si substrates and nanomaterials/nanostructures on top of graphene field-effect transistors.

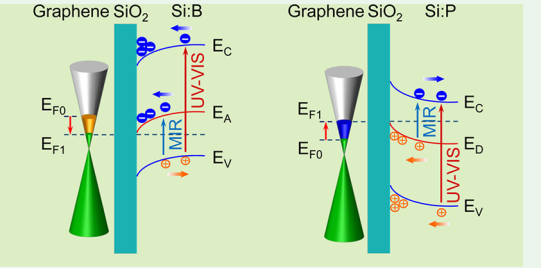

KEYWORDS: *shallow impurity states, mid-infrared photodetectors, photogating effect, doped silicon, nanostructures, and graphene*

INTRODUCTION

The capabilities of mid-infrared photodetection are highly desirable for many applications such as spectroscopy, chemical and biomolecular sensing, infrared imaging, night vision, security, and industry.[1,2] Silicon (Si) photodetectors based on complementary metal-oxide-semiconductor (CMOS) technology are of low cost and have maturity, high performance, and high level of integration with electronics from the deep ultraviolet (UV) to near-infrared (IR) region. Photodetection beyond the near-IR region typically is based on either thermal photodetection (i.e., pyroelectric, bolometer, thermocouple, and thermopile detectors), narrow band gap semiconductors (i.e., InSb, InGaAs, and HgCdTe detectors), or photoionization of shallow impurities (i.e., block-impurity bands using Si:Ga, Si:B, and GaAs:Te detectors).[3−5] Thermal photodetectors have low sensitivity, have a long response time, and often require human intervention. The other photodetectors require cryogenic operation and complicated fabrication processes that are only accessible for small-volume and high-value markets and cannot compensate for the demands of markets such as Si detectors.

Recently, numerous efforts have been devoted to realizing mid-IR photodetectors by utilizing unique properties of graphene and nanostructures/nanomaterials. The former has a zero-band gap, enabling ultra-broadband photodetection from the deep UV to terahertz region and high carrier mobility, allowing for high operating speed. However, the intrinsic weak photon absorption in graphene limits the photoresponsivity of these photodetectors based on graphene-metal or graphene p−n junctions on the scale of mA/W.[6−9] The latter enhances the absorption via nanostructures (i.e., metallic plasmonics and microcavities)[10−13] and nanomaterials (i.e., colloidal quantum dots (CQDs)).[14,15] Hybrid graphene-CQD photodetectors have been obtained with high responsivity, in which CQDs are used as absorbers. However, the relatively large band gap of CQDs restricts the operation of the photodetectors beyond the near-IR region.[14,15] Recently, by exploiting intraband transitions of heavily doped PbS CQDs, these devices can detect photons in the mid-IR region with a low responsivity (∼0.15 mA/W),[16] or by employing narrow band gap HgTe CQDs with graphene, the photodetectors have a spectral sensitivity beyond 3 μm.[17] However, these photodetectors operate at low temperatures (80 K).[16,17] All of them place an impediment in the path toward the advancement of mid-IR photodetectors at room temperature.

It is thus worth considering other approaches that can be utilized in realizing photodetection in the mid-IR regime. We have demonstrated a prospective approach for high photoresponsivity from pure graphene in the mid-IR region at room

Received: May 8, 2022
Accepted: July 20, 2022
Published: August 15, 2022

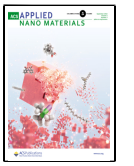

https://doi.org/10.1021/acsanm.2c02011
ACS Appl. Nano Mater. 2022, 5, 12477−12486

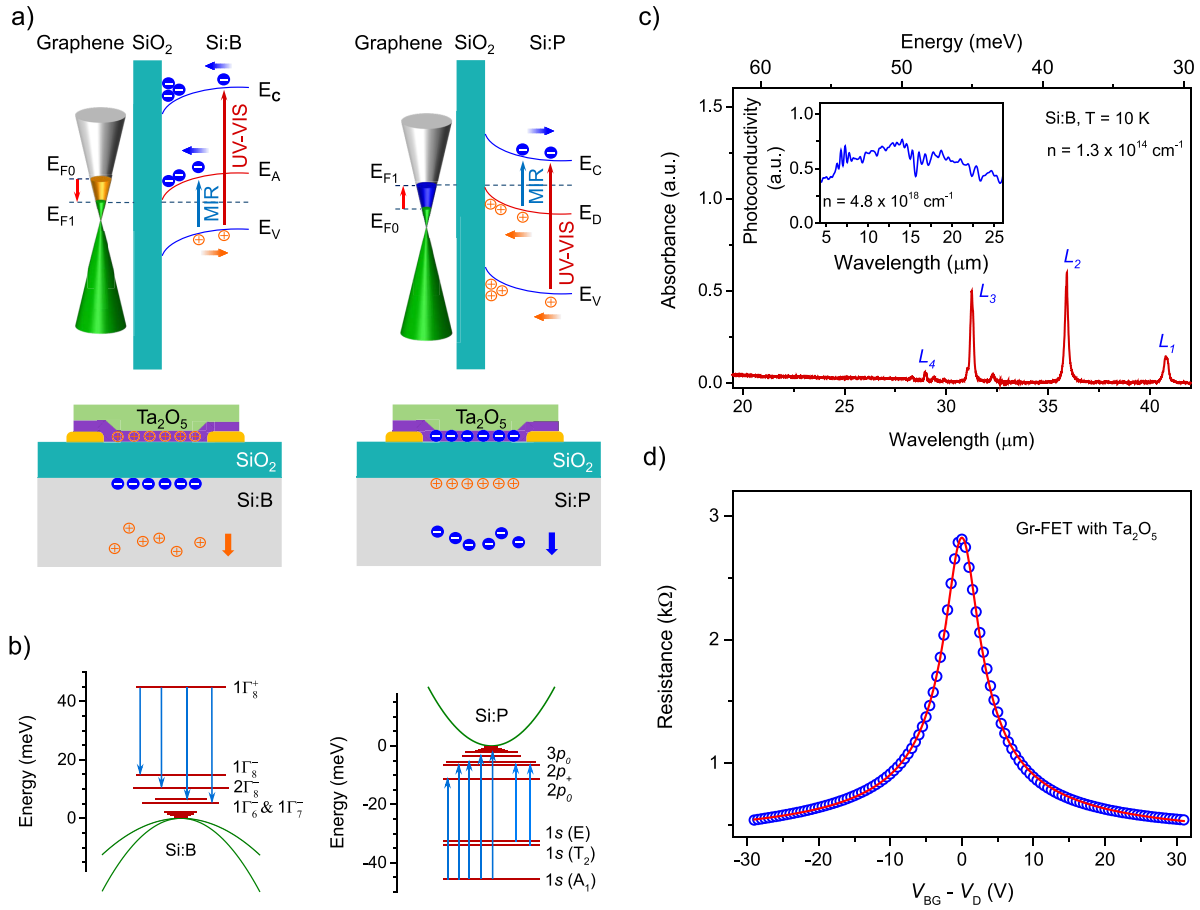

Figure 1. Performance of Gr-FET photodetectors based on the photogating effect for both n-type and p-type Si substrates. (a) Energy band diagrams of heterostructures of Gr/SiO_2/Si:B (left-top) and Gr/SiO_2/Si:P (right-top), and the shift of the Fermi level of graphene is induced by the accumulation of photogenerated carriers at the Si/SiO_2 interface under illumination. Schematic diagrams of the Gr-FET photodetectors on Si:B (left-bottom) and Si:P (right-bottom) substrates (gray) include ALD Ta_2O_5, graphene (purple), source and drain electrodes (yellow), and SiO_2/Si layers. Blue dots are electrons, and orange dots are holes. (b) Schematics of energy levels and optical transitions from ground states to excited states of shallow impurities in Si:B and Si:P are illustrated. (c) Absorption spectrum for Si:B at 10 K indicates optical transitions in the Si:B material. The inset shows a photoconductivity response spectrum of highly doped Si:B at 10 K. (d) Resistance−voltage characteristics of a Gr-FET photodetector on the Si:B substrate (n = 4.6 × 10^{19} cm^{-3}) with an ALD Ta_2O_5 capping layer under V_{DS} = 0.1 V have been used to estimate the high carrier mobility of graphene.

temperature. Here, p- and n-type doped Si wafers are utilized as an efficient absorber in the mid-IR region via shallow impurity bands from boron (B) and phosphorus (P)-doped Si, respectively, instead of only supporting a segment of photodetectors. The mismatch of the work function between Si and SiO_2 with graphene creates a potential well to capture photogenerated carriers (electrons or holes) at the Si/SiO_2 interface, inducing an additional voltage to modulate the carrier concentration of the graphene channel through the capacitive coupling. The carriers in the graphene channel possess very high mobility. These factors lead to a high gain of photocurrent in the graphene field-effect transistor (Gr-FET) photodetectors.

The key to obtain high performance of planar optoelectronic chips which are compatible with silicon technology is the quality of interfaces between difference materials. The success of the planar-silicon-device technology is derived from the chemically and mechanically stable SiO_2, near-ideal Si/SiO_2 interface, and well-controlled doping process in Si, which provide a very low trap concentration at the Si/SiO_2 interface.[18−21] For Gr-FET, other traps associated with the graphene channel cause the degradation of the carrier mobility due to the long-range Coulomb scattering.[22,23] To overcome the issues, a Ta_2O_5 thin film has been grown atop the graphene channel. Thanks to the screening effect of the layer with a high-κ dielectric constant (κ = 25−50) that can suppress the long-range scattering, resulting in increasing carrier mobility observed in several reports.[24,25] Thus, the high-κ dielectric layer introduced as a capping layer of the graphene channel provides an important factor to the performance of our photodetectors and protects our devices from atmospheric contaminants. In addition, the development in the growth of commercial wafer-scale graphene enables transferring graphene on large Si wafers, thus suitable for monolithic integration with silicon-integrated circuits based on CMOS technology.[26,27] The configuration provides a promising way for photodetectors based on other two-dimensional (2D) materials (i.e., MoS_2, $MoTe_2$, WS_2, and black phosphorus) in the mid-IR region and a new concept of the dual-photogating effect induced by both the doped Si substrate and absorber layer[28,29] on top of the 2D material channel. The contribution of substrates such as Si to the performance of the photodetectors based on 2D materials should be contemplated.

https://doi.org/10.1021/acsanm.2c02011
ACS Appl. Nano Mater. 2022, 5, 12477−12486

To elucidate the effect of doping concentration in Si substrates on the performance of the graphene photodetectors, we have systematically investigated the photoresponse of the Gr-FET photodetectors on both p- and n-type Si substrates (Si:B and Si:P, respectively) with different doping concentrations under light illumination from the deep UV to mid-IR region. The Gr-FET photodetectors on lightly doped Si substrates achieve the highest performance under the deep UV, visible, and near-IR illumination. In contrast, the Gr-FET photodetectors on the highly doped Si substrates demonstrate the best performance under a mid-IR illumination of 10.6 μm with a photoresponsivity of 5 A/W and a fast rise time of <4.2 ms. Primarily, we have focused on the photoresponse of Gr-FETs at the mid-IR region.

Fabrication and Characterization. We have fabricated Gr-FETs on both p-type boron-doped silicon (Si:B) and n-type phosphorus-doped silicon (Si:P) substrates with three different doping concentrations of 3×10^{15}, 4.8×10^{18}, and 4.6×10^{19} cm^{-3} that are below the Mott critical concentration toward the metallic state.[30] First, an 80 nm dry thermal SiO_2 layer was grown on these Si wafers at 1100 °C. Drain, source, and back-gate contacts (5 nm Cr and 100 nm Au) were created using photolithography, electron-beam (e-beam) evaporation, and metal lift-off processes. After that, a monolayer graphene layer was transferred to the Si/SiO_2 substrates. Photolithography and oxygen-plasma etching were employed to define the graphene channel with a drain-to-source distance, L, of 6 μm, and a width, W, of 15 μm. A 2 nm Ta_2O_5 nucleation layer was grown on top of the graphene channel by the e-beam evaporation method. Finally, a 30 nm Ta_2O_5 film was grown on the devices by the atomic layer deposition (ALD) method.

The photoresponse characteristics of the Gr-FET detectors with and without light illumination at room temperature were characterized by source-meter units. A Keithley 2450 was used to set a drain-source bias, V_{DS}, of 100 mV and to collect the drain current, I_D, while the other Keithley 2450 was employed to control the back-gate bias, V_{BG}, from −30 to 30 V. Several light sources with wavelengths of 532 nm, 1.5 μm, 4.55 μm, 8.5 μm, and 10.6 μm and an Edmund tungsten lamp providing a visible to near-IR source were used to characterize the photoresponse of the devices. The continuous laser beams were switched ON/OFF by the mechanical chopper and acousto-optic modulator (AOM). The details of the fabrication process and characterization of the Gr-FET photodetector are presented in the Supporting Information.

RESULTS AND DISCUSSION

The performance of Gr-FET photodetectors based on the photogating effect for both p- and n-type Si substrates under over band gap excitation and photoionization with illumination of UV to near-IR and mid-IR, respectively, is illustrated in Figure 1a. The energy of conduction and valence bands of Si localizes in the range from −5.13 to −4.01 eV.[31] The work function of p-type (Si:B), n-type (Si:P) and graphene is about 5.07, 4.14 and 4.56 eV, respectively.[31−34] Therefore, a difference in the work function between SiO_2 and doped Si materials in the structure with graphene results in the bending of the energy bands, namely, downward for p-type (Si:B) or upward for n-type (Si:P) materials at the Si/SiO_2 interface. For the Si:B substrate, the downward band bending creates a potential well for electrons at the interface. Depending on the photon energy, electrons in the valence band are excited to the conduction band by the over band gap excitation (E_{ex} > 1.1 eV) or the photoionization of acceptor centers under mid-IR illumination, leaving holes behind in the valence band. Due to the interfacial potential, electrons (blue dots) are accumulated at the Si/SiO_2 interface, while holes (orange dots) are repelled to the bulk Si and then ended at the back gate. The confinement of the photogenerated electrons in the potential well provides an additional negative bias at the Si/SiO_2 interface that induces extra holes in the graphene channel by the capacitive coupling effect through the dielectric SiO_2 layer. The Fermi level of graphene is, thus, shifted downward from E_{F0} to E_{F1} (Figure 1a). Due to the high mobility of carriers in graphene, holes in the graphene channel are recirculated as long as the electrons are trapped at the interface under a bias voltage between the drain and source, V_{DS}. As a result, a gain of the photocurrent in such Gr-FET photodetectors is obtained. Similarly, for the n-type substrate, holes are trapped at the Si/SiO_2 interface due to the interfacial potential. The capacitive coupling effect via the SiO_2 layer will shift the Fermi level of graphene upward from E_{F0} to E_{F1}, which implies an increase in electron density in the graphene channel. When an electron in the graphene channel reaches the drain, another electron is induced from the source due to charge conservation. This gives rise to a photoconductive gain or a high photocurrent and photoresponsivity of the Gr-FET photodetectors on the n-type Si substrate.

The devices detect photons in a large range of wavelength from the deep UV to mid-IR region and strongly depend on a number of parameters of fabrication. The photoresponse of Gr-FET photodetectors on the Si:B substrate (3×10^{15} cm^{-3}) with and without a high-κ dielectric Ta_2O_5 capping layer has been explored under visible illumination. The screening effect of the high-κ dielectric Ta_2O_5 layer can minimize the degradation of carrier mobility in graphene,[24,25,35] contributing to the high performance of these photodetectors, which will be discussed in the following paragraphs. In the visible region, The Gr-FET photodetectors on the Si:B substrate with the Ta_2O_5 layer show a high photoresponsivity of $\sim 1.2 \times 10^6$ A/W, around two times higher than that without a Ta_2O_5 layer of $\sim 5.4 \times 10^5$ A/W (Figure S6). When the doping concentration of Si wafers increases from 3.0×10^{15} to 4.6×10^{19} cm^{-3}, the photoresponsivity decreases in the visible region. Here, we focus on the photodetection in the mid-IR region, and results for the photodetection in the visible region are provided in the Supporting Information.

Under mid-IR illumination, shallow impurities in Si:B and Si:P substrates are photon-ionized and a photocurrent has been observed. Fourier-transform infrared (FTIR) spectra were obtained using a Bruker Vertex 80v spectrometer with a resolution of 0.15 cm^{-1} from Si:B and Si:P samples at 10 K. Narrow absorption lines including L_1, L_2, L_3, and L_4 of boron impurities (Si:B sample) have been observed in a low doping concentration material of 1.3×10^{14} cm^{-3}, corresponding to electric dipole transitions from the ground state, $1\Gamma_8^+$, to excited states $1\Gamma_8^-$, $2\Gamma_8^-$, $1\Gamma_6^-$, and $1\Gamma_7^-$ (Figure 1b). For Si:P samples, a number of narrow absorption lines, including I_1, I_2, I_3, I_4, I_5, I_6, and I_7 related to Lyman transitions from the ground state, $1s(A_1)$, to excited states np_0 and $np_\pm$ (i.e., n = 2, 3, 4...), have been observed in the range of 20−52 μm (Figure S3). The shallow acceptor or donor centers have been photoionized under the mid-IR radiation, generating free holes or electrons, respectively. The photoconductive response of a highly doped Si:B sample (4.8×10^{18} cm^{-3}) was collected using the FTIR spectrometer from 4.5 to 26 μm (inset, Figure 1c). The

https://doi.org/10.1021/acsanm.2c02011
ACS Appl. Nano Mater. 2022, 5, 12477−12486

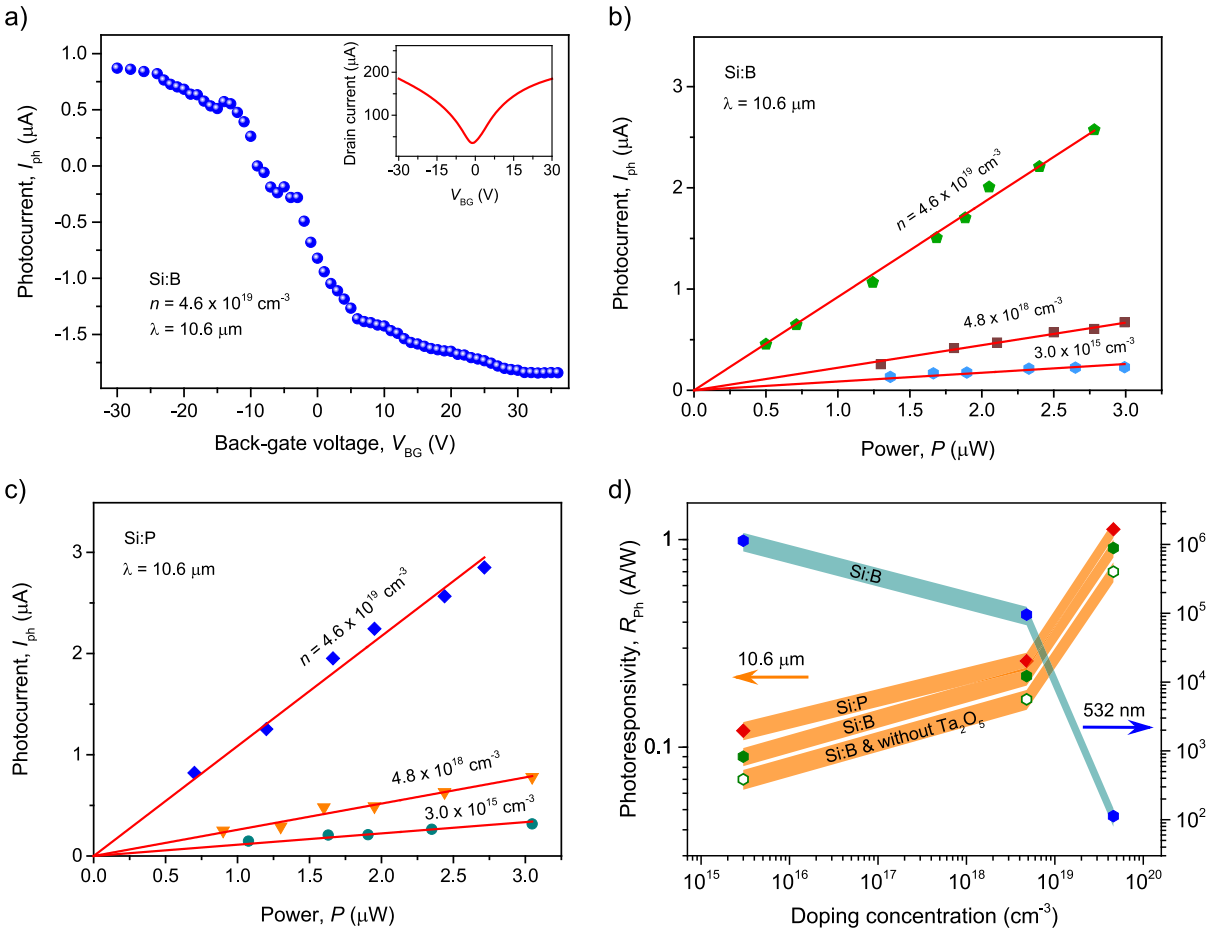

Figure 2. Photoresponse characterization of Gr-FET photodetectors at room temperature and under V_{DS} = 0.1 V. (a) Photocurrent depends strongly on the back-gate voltage from a Gr-FET on a highly doped Si:B substrate ($n = 4.6 \times 10^{19}$ cm^{-3}) with an ALD Ta_2O_5 capping layer under 10.6 μm illumination. The inset shows a current−voltage (I−V) characteristic of this Gr-FET. (b) & (c) Si substrates with high doping concentration provide higher efficiency for the photon−carrier conversion, indicating from the photocurrent as a function of 10.6-μm illumination power of Gr-FETs on Si:B and Si:P substrates with an ALD Ta_2O_5 capping layer, respectively, under V_{BG} = −27 V. (d) Behavior of photoresponsivity of Gr-FETs on Si:B and Si:P substrates with and without an ALD Ta_2O_5 capping layer is different under 10.6 μm (left axis) and 532 nm (right axis) illumination.

photoconductivity response spectra have been observed in doped semiconductors, namely, Si:P,[36] Si:Sb,[37] Si:As,[38] and Si:B,[3] with the photoconductivity response range up to 40 μm and the photoresponse range for Ge:Sb,[39] Ge:B,[40] and GaAs:Te[5] up to 300 μm. When the concentration of impurity increases, the photoconductivity response extends to the longer wavelength because of the broadening of the impurity band.[3,37,41,42] In this work, we have fabricated devices on highly doped Si:B and Si:P substrates that the photoconductive response of shallow impurity bands starts from 4.5 μm, increases to the highest value at ∼ 13.5 μm, and extends up to 26 μm (inset, Figure 1c). Such photogenerated carriers from the impurity bands under mid-IR radiation will be accumulated at the Si/SiO_2 interface, leading to a gain of photocurrent in the graphene channel of Gr-FETs.

The carrier mobility of graphene is an important factor for the performance of Gr-FET photodetectors based on the photogating effect.[43−46] The carrier mobility of graphene in Gr-FETs without a dielectric capping layer is reported typically from 1600 to 4500 cm^2 V^{-1} s^{-1}, which is much lower when compared with those in a free-standing graphene sheet.[43−45,47] The degradation of carrier mobility related to the long-range Coulomb scattering can be governed by a screening effect of a high-κ dielectric layer grown on the graphene channel of the Gr-FETs. A number of experimental reports on the screening effect of high-κ dielectric materials with a dielectric constant, ε, of ∼20−45 have shown the preservation of the carrier mobility in Gr-FETs.[24,25,35] In addition, the dielectric capping layer protects our devices from atmospheric contaminants so that the devices operate stably for more than 1 year in our normal condition.

To obtain high mobility of carriers in graphene, we have grown a high-κ dielectric Ta_2O_5 film (ε ∼ 25−50) on the graphene channel by the ALD method.[29,35,48−50] The ALD Ta_2O_5 capping layer does not provide any photogenerated carriers for the graphene channel under light illumination, confirmed by the absorption spectra from the deep UV to mid-IR region. No absorption peak from the deep UV to near-IR region has been observed, and only an absorption band in the deep UV (<300 nm) typically corresponds to deep electron traps from oxygen vacancies in Ta_2O_5 films.[51,52] In the near to mid-IR region (up to 20 μm), several absorption peaks are assigned to lattice vibrational modes.[53,54] Thus, the ALD Ta_2O_5 film does not induce a photocurrent in the Gr-FETs from the deep UV to mid-IR region. The carrier mobility, μ, can be extracted from resistance−voltage characteristic curves

https://doi.org/10.1021/acsanm.2c02011
ACS Appl. Nano Mater. 2022, 5, 12477−12486

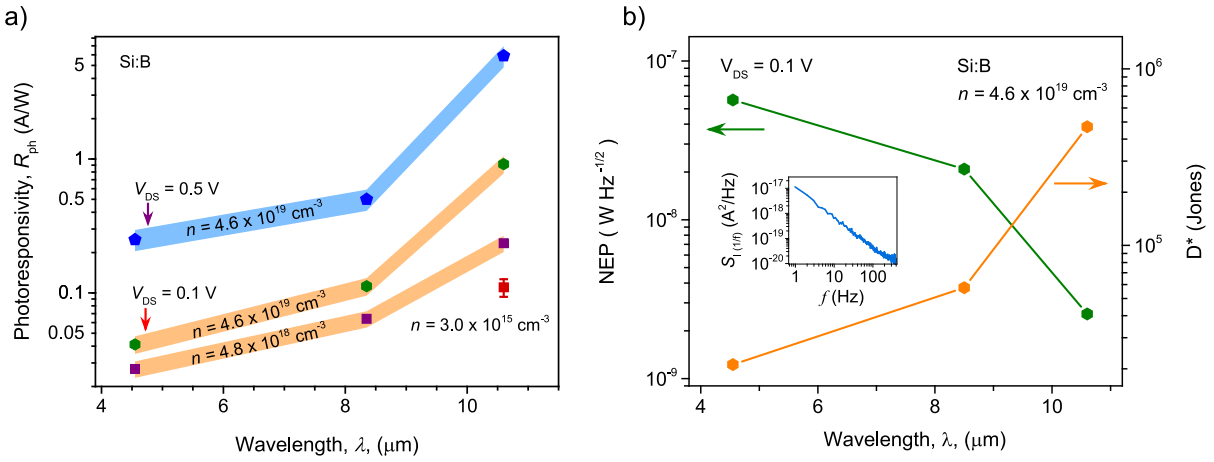

Figure 3. Wavelength dependence of Gr-FET photodetectors at room temperature. (a) Photoresponsivity of Gr-FETs on the Si:B substrate increases as wavelength gets longer from 4.55 to 10.6 μm under V_{DS} = 0.1 V. (b) Noise-equivalent-power (NEP) and specific detectivity (D^*) of the Gr-FETs on the Si:B substrate (n = 4.6 × 10^{19} cm^{-3}) have been estimated. The inset shows the noise-power spectral density of the 1/f noise.

of the Gr-FETs with an ALD Ta_2O_5 capping film by fitting to the expression.[55−57]

$$R = R_c + R_{ch} = R_C + \frac{L/W}{e\mu\sqrt{n_0^2 + \left(\frac{C_G}{q}(V_{BG} - V_{Dirac})\right)^2}} \quad (1)$$

where R is the total resistance, R_c is the total contact resistance, R_{ch} is the graphene channel resistance, e is the elementary charge, $C_G = \frac{\varepsilon\varepsilon_0}{d} \sim 43.2$ nF/cm^2 is the gate capacitance per unit area, d = 80 nm is the SiO_2 thickness, ε_0 is the vacuum permittivity, ε = ∼3.9 is the dielectric constant of SiO_2,[58] n_0 is the carrier concentration induced by charged impurities at the graphene/SiO_2 interface, and $n_g = \frac{C_G}{q}(V_{BG} - V_{Dirac})$ is the carrier concentration generated by the back-gate voltage away from the Dirac point voltage, V_{Dirac}. The red curve shows the best fit to the resistance−voltage characteristic curve with a carrier mobility of ∼10,538 cm^2 V^{-1} s^{-1} (Figure 1d).

We have characterized the photoresponse of the Gr-FET photodetectors on both p-type Si:B and n-type Si:P substrates with different doping concentrations under mid-IR illumination from a 10.6 μm CO_2 laser and V_{DS} = 0.1 V. A current−voltage (I−V) characteristic curve from a Gr-FET on a Si:B substrate with a high doping concentration (4.6 × 10^{19} cm^{-3}) is plotted in the inset of Figure 2a. The photocurrent as a function of back-gate voltage under an illumination power of 2.7 μW is shown in Figure 2a. The signals collected from Gr-FETs on Si:B substrates with different doping concentrations are plotted as a function of illumination power from 0.5 to 3.0 μW at 10.6 μm and under V_{BG} = −27 V (Figure 2b). The photocurrent grows linearly with increasing light intensity. Similarly, we also have observed a linear behavior of photocurrent for Gr-FETs on Si:P substrates (Figure 2c). The linear dependence of the photocurrent with light intensity shows evidence that the thermal effect induced by oxide layers do not contribute significantly to the electrical current of the devices.

The higher the doping concentration is in Si substrates, the higher the photocurrent and photoresponsivity have been obtained for both p- and n-type materials under mid-IR illumination. In this case, mid-IR photons have enough energy to photoionize holes from boron acceptor centers to the valence band of a Si:B substrate or electrons from phosphorus donor centers to the conduction band of a Si:P substrate. The distance between impurities reduces in highly doped silicon wafers, so wave functions of holes or electrons are overlapped. The discrete levels of acceptor and donor impurities widen and become impurity bands, which will increase the transition probability of holes or electrons under the mid-IR radiation. Therefore, higher doping concentration in Si substrates will have higher efficiency for the photon−carrier conversion than lower ones, resulting in a higher gain of photocurrent in the Gr-FET photodetectors (Figure 2b,c).

The gain of the photocurrent strongly depends on the carrier mobility of graphene and doped silicon materials. With increasing doping concentration in Si:B substrates from 3 × 10^{15} and 4.8 × 10^{18} to 4.6 × 10^{19} cm^{-3}, the photoresponsivity increases from ∼0.09 to ∼0.22 and ∼0.91 A/W and ∼0.07, ∼0.17, and ∼0.70 A/W for the Gr-FETs with and without an ALD Ta_2O_5 capping layer, respectively (Figure 2d). The results show that the high-κ dielectric layer covering the graphene channel has assisted an important role in preserving the high carrier mobility of graphene via the screening effect. Furthermore, the Gr-FETs with and without the Ta_2O_5 cap layer on the n-type Si:P substrates provide higher photocurrent (Figures 2b,c and S8) and photoresponsivity (Figures 2d and S10) than those on the p-type Si:B substrates with the same doping concentrations. The carrier mobility in Si:P is higher than that of Si:B, about a factor of 2 under highly doping concentration.[59,60] Thus, photogenerated carriers in Si:P are separated faster than that in Si:B, and the additional voltage at the interface will be built up with higher efficiency in the Si:P substrate under the same illumination condition. This explains the difference in the photoresponsivity in two types of Si substrates by ∼ 23% under 10.6 μm mid-IR illumination (Figure 2d). Specifically, the Gr-FETs with the Ta_2O_5 cap layer on the Si:P substrates demonstrate the photoresponsivity from 0.12 to 1.12 A/W, which corresponds to the doping concentration from 3 × 10^{15} to 4.6 × 10^{19} cm^{-3}.

In contrast, the higher doping concentration in either the p- or n-type doped Si substrate leads to a lower photocurrent and photoresponsivity under the over band gap excitation (λ = 532 nm, Figure 2d). Specifically, the photoresponsivity reduces rapidly from 1.2 × 10^6 to 9.5 × 10^4 and 1.1 × 10^2 A/W with

https://doi.org/10.1021/acsanm.2c02011
ACS Appl. Nano Mater. 2022, 5, 12477−12486

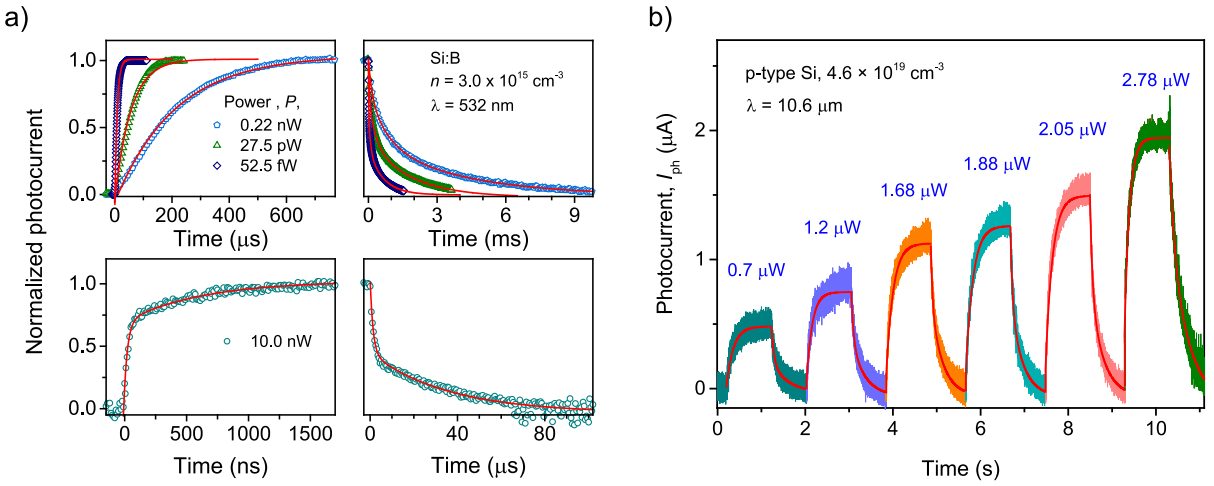

Figure 4. Response time of Gr-FET photodetectors at room temperature on the Si:B substrate at room temperature under V_{DS} = 0.1 V. (a) Under 532 nm irradiation and V_{BG} = 3.5 V and (b) under 10.6 μm illumination and V_{BG} = −27 V.

increasing doping concentration in Si:B substrates from 3 × 10^{15} cm^{-3} to 4.8 × 10^{18} and 4.6 × 10^{19}, respectively. The reduction of the photoresponsivity is originated from the lifetime of photogenerated carriers. The carrier lifetime in Si substrates is strongly governed by recombination processes, including band-to-band and trap-assisted recombination.[61−63] For the band-to-band recombination, energy released through the recombination process of an electron from the conduction band with a hole in the valence conduction band radiates a photon (radiative recombination), transfers to another free carrier (Auger recombination), or is absorbed by the lattice. The radiative recombination has a low probability in indirect band gap materials such as Si. The Auger recombination process becomes a dominant process for doped Si materials with its rate proportional to the square of the doping concentration.[61,63] The trap-assisted recombination is related to a number of defects (i.e., dangling bonds) at the Si/SiO_2 interface with its rate proportional to the doping impurity concentration.[61,63] Therefore, fast recombination of electrons and holes associated with the high doping level in Si will lead to fewer photogenerated carriers reaching the Si/SiO_2 interface. This explains the fact that photocurrent and photoresponsivity are reduced in devices with highly doped Si substrates under the over band gap excitation.

Furthermore, we have investigated the dependence of the Gr-FETs' photoresponsivity on the wavelength from the deep UV to mid-IR region. The photoresponsivity in the deep UV to near-IR region reaches a maximum of ∼3 × 10^6 A/W at 700 nm, as discussed in the Supporting Information (Figure S6d).[29] Here, we focus on the photoresponsivity in the mid-IR region. The photocurrent of Gr-FETs on highly doped Si:B substrates was collected under different illumination powers of mid-IR light sources with wavelengths of 4.55, 8.5, and 10.6 μm (Figure 3a, S9, and 2b). The photoresponsivity increases as wavelength gets longer from 4.55 to 10.6 μm under V_{DS} = 0.1 V. The results follow the photoconductivity spectrum of the Si:B substrate in our measurements (Figure 1b) and other observations,[3,36] in which the photoconductivity increases from 4.55 to 10.6 μm. In highly doped Si substrates, discrete donor and acceptor impurity levels broaden and become impurity bands; thus, the photoionization cross-section is proportional to the doping concentration. As a result, the photoresponsivity increases with increasing doping concentration. Specifically, Gr-FETs on the lightly doped Si:B substrate (3.0 × 10^{15} cm^{-3}) only show a photoresponsivity of ∼0.11 A/W under 10.6 μm excitation, and no photoresponse under 4.55 and 8.5 μm excitation (Figure 3a) has been observed. However, Gr-FETs on highly doped Si substrates (4.8 × 10^{18} and 4.6 × 10^{19} cm^{-3}) can detect mid-IR photons for all the three light sources with high photoresponsivity. For example, under 10.6 μm illumination, the photoresponsivity is ∼1 and ∼5 A/W for V_{DS} = 0.1 and 0.5 V, respectively (Figure 3a).

To evaluate the performance of the Gr-FET photodetectors, the noise equivalent power (NEP) and specific detectivity (D^*) for the Gr-FETs on highly doped Si:B substrates can be estimated by $\mathrm{NEP} = \sqrt{S_I(1/f) + S_I(\mathrm{shot}) + S_I(\mathrm{thermal})}/R_{ph}$ and $D^* = \sqrt{A}/\mathrm{NEP}$, where A is the area of the graphene channel, $S_I(1/f)$, $S_I(\mathrm{shot})$, and $S_I(\mathrm{thermal})$ are the power spectral density of the $1/f$ noise, shot noise, and thermal noise of about 5.4 × 10^{-18}, 1.25 × 10^{-23}, and 6.55 × 10^{-25} A^2/Hz, respectively, at V_{DS} = 0.1 V for 1 Hz bandwidth.[35,64,65] The power spectral density of the $1/f$ noise is presented in Figure 3b, inset. The NEP values of the photodetector are between 5.7 × 10^{-8} (at λ = 4.55 μm) and 3.3 × 10^{-9} W $Hz^{-1/2}$ (at λ = 10.6 μm). The specific detectivity, D^*, ranges from 2.1 × 10^4 to 3.6 × 10^5 Jones (cm $Hz^{1/2}$/W), as presented in Figure 3b. Details of the NEP and D^* under V_{DS} = 0.1 and 0.5 V are discussed in the Supporting Information.

To gain insights into the operating speed of the photodetectors, we have characterized the response time under both visible and mid-IR illumination for the Gr-FETs on Si:B substrates. Under the over band gap excitation (E_{ex} > 1.1 eV), electrons are immediately excited to the conduction band, leaving behind free holes in the valence band. These carriers have high momentum and are quickly captured at the potential well at the Si/SiO_2 interface. A fast response time is expected for this excitation. Under the mid-IR irradiation, free carriers in silicon are generated by the photoionization process of shallow centers. These carriers will drift to the potential well. The process is slower compared with the over band gap excitation; thus, a slow response time is expected for the mid-IR excitation.

https://doi.org/10.1021/acsanm.2c02011
ACS Appl. Nano Mater. 2022, 5, 12477−12486

To explore the response time of our devices under the over band gap excitation, all measurements were performed at room temperature under V_{DS} = 0.1 V and V_{BG} = 3.5 V for visible irradiation. The response time is slow under a low illumination power (in the femto-watt level), and it becomes faster at higher illumination intensity (in the pico-watt regime). Specifically, the rise time and fall time (between 10 and 90% of the peak photocurrent) reduce from 410 to 8.2 μs and from 4.5 to 0.76 ms, respectively, when the illumination power of the 532 nm light source increases from 27.5 fW to 0.22 nW (Figure 4a, top). Under low-intensity illumination, photogenerated holes fill the potential well at the Si/SiO_2 interface[61,63] when they reach the surface. Holes fill slowly the potential well and contribute to an additional voltage of the photogating effect of the graphene channel. More electron−hole pairs are created with increasing light intensity, and electronic states in the well are diminished. Under high-illumination intensity, the potential well is quickly filled by holes, and extra photogenerated electron−hole pairs will be recombined immediately; thus, the saturation of photocurrent has been observed after a particular time. It means that under high intensity illumination, the rise time will reach the diffusion time of the carriers to the potential well at the Si/SiO_2 interface. Thus, the photodetectors demonstrate a fast operation speed with a rise time of 380 ns and a fall time of 220 μs under a high-power illumination of 10 nW (Figure 4a, bottom).

Looking in detail at the dynamics of the photodetectors, the rise time consists of two components at the nano-watt illumination, including a fast rise time, $\tau_{1R} \sim 20$ ns, and a slow one, $\tau_{2R} \sim 360$ ns (Figure 4a, bottom). The fast rise time corresponds to the carrier transit time in the graphene channel, while the slow component represents the average diffusion time of photogenerated carriers to the potential well at the Si/SiO_2 interface. The rise time of our Gr-FETs in the visible region is several orders of magnitude faster than those reported in previous observations.[14,15,66−69] The experiment results also show that the fall time includes two components. The fast fall-time constant, $\tau_{1F} \sim 500$ ns, is similar to the slow rise time, which can be originated from the average diffusion time of photogenerated carriers out of the potential well at the Si/SiO_2 interface after the light is turned off. The slow fall-time constant, $\tau_{2F} \sim 42$ μs, is resulted from carrier traps (i.e., dangling bonds) in SiO_2 near the Si/SiO_2 interface. Fitting the response time is described in the Supporting Information.

The response time of the Gr-FETs on highly doped substrates under mid-IR illumination has been investigated, exploring the photoionization process of shallow impurities. The red curves present the best fit of the photoresponse time under different illumination intensities of the 10.6 μm illumination and V_{BG} = −27 V (Figure 4b). The rise time and fall time are ∼170 and ∼420 ms, respectively, under low illumination power. The shortening of the rise time and fall time has been observed under high illumination intensity (2.78 μW), where the rise time has two components of $\tau_{1R} \sim 4.2$ ms and $\tau_{2R} \sim 180$ ms, and the fall time also has two components of $\tau_{2F} \sim 90$ ms and $\tau_{2F} \sim 400$ ms. The difference in the operating speed under the visible and mid-IR illumination can come from their excitation mechanisms. The excitation cross-section of the above-band gap illumination (λ = 532 nm) is several orders of magnitude higher than that of the below-band gap excitation (λ = 10.6 μm). Thus, fewer electrons and holes are generated under the mid-IR illumination when compared with those under the visible irradiation with the same photon flux. Electronic states in the potential well at the Si/SiO_2 interface need a longer time to be filled under the mid-IR illumination due to fewer photogenerated carriers. Therefore, low efficiency in filling electrical states at the potential well under the below-band gap excitation has caused the slow response speed in the mid-IR region.

To integrate these photodetectors into a 2D array for digital cameras, the active area should be small within a pixel size of a few microns. The active area of each photodetector needs to be characterized. Photogenerated carriers contributed to the photogating effect have been generated in the Si substrate. It is important to know how far away from the graphene channel these carriers can contribute to the photogating effect. We fabricated Gr-FETs isolated by an enclosed canal with a width of 5 μm and a depth of 15 μm. SEM images of these structures are shown in Figure 5 and S13. The distance, r, from the edge

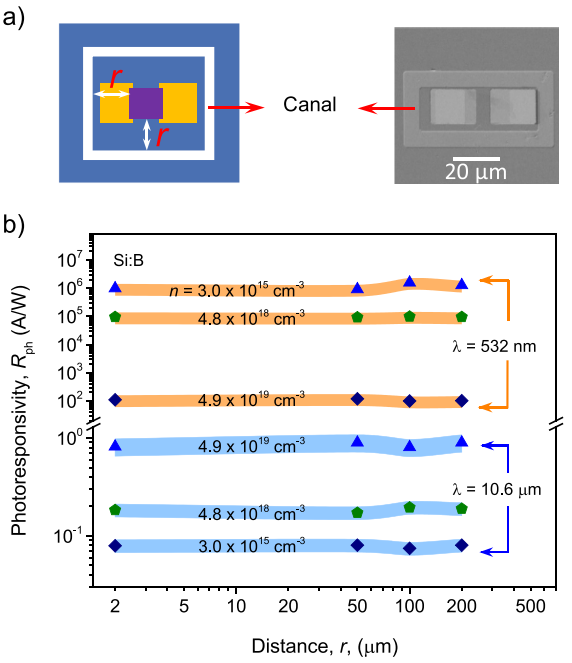

Figure 5. The spatial dependence of photoresponsivity of Gr-FET photodetectors. (a) Schematic and SEM image show a Gr-FET isolated by a canal, in which r is the distance from the graphene channel to the canal. (b) Photoresponsivity of the Gr-FETs on the Si:B substrate with an ALD Ta_2O_5 capping layer does not depend on the distance between the graphene channel and canal under 10.6 μm and 532 nm illumination.

of the graphene channel to the canal is varied from 2 to 50, 100, and 200 μm. We illuminated the Gr-FET photodetectors with a homogeneous beam instead of a focusing beam. Thus, only photogenerated carriers inside the canal can spatially diffuse to the area below the graphene channel, contributing to the photogating effect. However, the photoresponsivity of the Gr-FETs does not change when we vary the distance between the graphene channel and canal under both 532 nm and 10.6 μm illumination (Figure 5b). These results point out that no lateral carrier diffusion has been observed in these structures. Carriers far from the graphene channel do not contribute to the photoresponse, in contrast to previous reports.[43,70] Under the 532 nm illumination, the penetration depth of the light in Si is less than 2 μm;[71] thus, photogenerated electrons and holes should be close to the Si/SiO_2 interface, about ≤2 μm.

https://doi.org/10.1021/acsanm.2c02011
ACS Appl. Nano Mater. 2022, 5, 12477−12486

An estimation of diffusion length of carriers in a lightly doped p-Si without an applied electrical displacement field is about several hundred microns;[43] these photogenerated carriers can diffuse in the lateral direction to the Si/SiO_2 interface. Using the canal configuration, we have proved that the lateral diffusion of photogenerated carriers is not contributed to the photoresponse of these detectors. Furthermore, the back-gate bias applied globally on the Si substrate and the built-in electrical field at the Si/SiO_2 interface result in an electric displacement field perpendicular to the interface. These electric fields drive carriers in the vertical direction. The electric displacement field caused by the drain-source voltage (~0.1 V) in the lateral direction is much weaker than that of the back-gate voltage varied from −30 to +30 V. Thus, the lateral diffusion of carriers is not an important factor for the photoresponse. Under the 10.6 μm illumination, photons can penetrate deeper in the Si substrate and generate carriers in bulk Si. The carriers cannot diffuse laterally toward the Si/SiO_2 interface area below the graphene channel. Most photogenerated carriers far from the graphene channel are recombined before reaching the potential well. Therefore, only photogenerated carriers below the graphene channel mainly contribute to the photogating effect under the visible and mid-IR illumination.

CONCLUSIONS

In summary, we have demonstrated the approach to obtain the high performance of broadband photodetectors sensitive to UV, visible, to mid-IR light based on the ultrafast carrier mobility of graphene and photoionization of shallow impurities in the highly doped Si:B and Si:P substrates. The recent developments in silicon technology, wafer-scale graphene, and growing high-κ semiconductor materials have provided a low trap concentration in nanostructures; thus, remarkable achievements for mid-IR photodetection have been obtained in hybrid silicon devices. We have observed graphene photodetectors on silicon with a photoresponsivity of ~5 A/W under the mid-IR illumination and $\sim 3 \times 10^6$ A/W in the visible to near IR region at room temperature. This approach can form a roadway for a concept of dual-photogating effect induced by both the highly doped Si substrate and absorber including nanostructures and nanomaterials on top of graphene field effect structures.

ASSOCIATED CONTENT

Supporting Information

The Supporting Information is available free of charge at https://pubs.acs.org/doi/10.1021/acsanm.2c02011.

Details for Gr-FET fabrication, optical and electrical setup, absorption spectra, photoresponse, and power spectral density of noises (PDF)

AUTHOR INFORMATION

Corresponding Author

Nguyen Q. Vinh − *Department of Physics and Center for Soft Matter and Biological Physics, Virginia Tech, Blacksburg, Virginia 24061, United States;* orcid.org/0000-0002-3071-1722; Phone: 1-540-231-3158; Email: vinh@vt.edu

Authors

Vinh X. Ho − *Department of Physics and Center for Soft Matter and Biological Physics, Virginia Tech, Blacksburg, Virginia 24061, United States;* orcid.org/0000-0001-5413-9030

Yifei Wang − *Department of Physics and Center for Soft Matter and Biological Physics, Virginia Tech, Blacksburg, Virginia 24061, United States*

Leslie Howe − *Department of Physics and Center for Soft Matter and Biological Physics, Virginia Tech, Blacksburg, Virginia 24061, United States*

Michael P. Cooney − *NASA Langley Research Center, Hampton, Virginia 23681, United States*

Complete contact information is available at: https://pubs.acs.org/10.1021/acsanm.2c02011

Notes

The authors declare no competing financial interest.

ACKNOWLEDGMENTS

The authors gratefully acknowledge the financial support of this effort by the Earth Science Technology Office (ESTO), NASA

REFERENCES

(1) Koppens, F. H. L.; Mueller, T.; Avouris, P.; Ferrari, A. C.; Vitiello, M. S.; Polini, M. Photodetectors based on graphene, other two-dimensional materials and hybrid systems. *Nat. Nanotechnol.* **2014**, *9*, 780−793.

(2) Wang, F.; Zhang, Y. B.; Tian, C. S.; Girit, C.; Zettl, A.; Crommie, M.; Shen, Y. R. Gate-variable optical transitions in graphene. *Science* **2008**, *320*, 206−209.

(3) Rauter, P.; Fromherz, T.; Winnerl, S.; Zier, M.; Kolitsch, A.; Helm, M.; Bauer, G. Terahertz Si:B blocked-impurity-band detectors defined by nonepitaxial methods. *Appl. Phys. Lett.* **2008**, *93*, 261104.

(4) Lynch, S. A.; Townsend, P.; Matmon, G.; Paul, D. J.; Bain, M.; Gamble, H. S.; Zhang, J.; Ikonic, Z.; Kelsall, R. W.; Harrison, P. Temperature dependence of terahertz optical transitions from boron and phosphorus dopant impurities in silicon. *Appl. Phys. Lett.* **2005**, *87*, 101114.

(5) Cardozo, B. L.; Haller, E. E.; Reichertz, L. A.; Beeman, J. W. Far-infrared absorption in GaAs : Te liquid phase epitaxial films. *Appl. Phys. Lett.* **2003**, *83*, 3990−3992.

(6) Park, J.; Ahn, Y. H.; Ruiz-Vargas, C. Imaging of Photocurrent Generation and Collection in Single-Layer Graphene. *Nano Lett.* **2009**, *9*, 1742−1746.

(7) Xia, F. N.; Mueller, T.; Lin, Y. M.; Valdes-Garcia, A.; Avouris, P. Ultrafast graphene photodetector. *Nat. Nanotechnol.* **2009**, *4*, 839−843.

(8) Xia, F. N.; Mueller, T.; Golizadeh-Mojarad, R.; Freitag, M.; Lin, Y. M.; Tsang, J.; Perebeinos, V.; Avouris, P. Photocurrent Imaging and Efficient Photon Detection in a Graphene Transistor. *Nano Lett.* **2009**, *9*, 1039−1044.

(9) Lemme, M. C.; Koppens, F. H. L.; Falk, A. L.; Rudner, M. S.; Park, H.; Levitov, L. S.; Marcus, C. M. Gate-Activated Photoresponse in a Graphene p-n Junction. *Nano Lett.* **2011**, *11*, 4134−4137.

(10) Echtermeyer, T. J.; Britnell, L.; Jasnos, P. K.; Lombardo, A.; Gorbachev, R. V.; Grigorenko, A. N.; Geim, A. K.; Ferrari, A. C.; Novoselov, K. S. Strong plasmonic enhancement of photovoltage in graphene. *Nat. Commun.* **2011**, *2*, 458.

(11) Engel, M.; Steiner, M.; Lombardo, A.; Ferrari, A. C.; Löhneysen, H. V.; Avouris, P.; Krupke, R. Light-matter interaction in a microcavity-controlled graphene transistor. *Nat. Commun.* **2012**, *3*, 906.

(12) Fang, Z. Y.; Liu, Z.; Wang, Y. M.; Ajayan, P. M.; Nordlander, P.; Halas, N. J. Graphene-Antenna Sandwich Photodetector. *Nano Lett.* **2012**, *12*, 3808−3813.

(13) Yao, Y.; Shankar, R.; Rauter, P.; Song, Y.; Kong, J.; Loncar, M.; Capasso, F. High-Responsivity Mid-Infrared Graphene Detectors with

Antenna-Enhanced Photocarrier Generation and Collection. *Nano Lett.* **2014**, *14*, 3749−3754.
(14) Ni, Z. Y.; Ma, L. L.; Du, S. C.; Xu, Y.; Yuan, M.; Fang, H. H.; Wang, Z.; Xu, M. S.; Li, D. S.; Yang, J. Y.; Hu, W. D.; Pi, X. D.; Yang, D. R. Plasmonic Silicon Quantum Dots Enabled High-Sensitivity Ultrabroadband Photodetection of Graphene-Based Hybrid Phototransistors. *ACS Nano* **2017**, *11*, 9854−9862.
(15) Konstantatos, G.; Badioli, M.; Gaudreau, L.; Osmond, J.; Bernechea, M.; de Arquer, F. P. G.; Gatti, F.; Koppens, F. H. L. Hybrid graphene-quantum dot phototransistors with ultrahigh gain. *Nat. Nanotechnol.* **2012**, *7*, 363−368.
(16) Ramiro, I.; Özdemir, O.; Christodoulou, S.; Gupta, S.; Dalmases, M.; Torre, I.; Konstantatos, G. Mid- and Long-Wave Infrared Optoelectronics via Intraband Transitions in PbS Colloidal Quantum Dots. *Nano Lett.* **2020**, *20*, 1003−1008.
(17) Grotevent, M. J.; Hail, C. U.; Yakunin, S.; Bachmann, D.; Calame, M.; Poulikakos, D.; Kovalenko, M. V.; Shorubalko, I. Colloidal HgTe Quantum Dot/Graphene Phototransistor with a Spectral Sensitivity Beyond 3 μm. *Adv. Sci.* **2021**, *8*, 2003360.
(18) Hattori, T.; Suzuki, T. Si-Sio2 Interface Structures on Si(100), (111), and (110) Surfaces. *Appl. Phys. Lett.* **1983**, *43*, 470−472.
(19) Helms, C. R.; Deal, B. E. *The Physics and Chemistry of SiO_2 and the Si-SiO_2 Interface*; Springer Science+Business Media: New York, 1988.
(20) Kasprzak, L. A.; Gaind, A. K. Near-Ideal Si-Sio2 Interfaces. *IBM J. Res. Dev.* **1980**, *24*, 348−352.
(21) Plummer, J. D.; Deal, D.; Griffin, P. B. *Silicon VLSI Technology: Fundamentals, Practice and Modeling*; US Ed Edition Pearson, 2000.
(22) Zhang, Y. B.; Brar, V. W.; Girit, C.; Zettl, A.; Crommie, M. F. Origin of spatial charge inhomogeneity in graphene. *Nat. Phys.* **2009**, *5*, 722−726.
(23) Hollander, M. J.; LaBella, M.; Hughes, Z. R.; Zhu, M.; Trumbull, K. A.; Cavalero, R.; Snyder, D. W.; Wang, X. J.; Hwang, E.; Datta, S.; Robinson, J. A. Enhanced Transport and Transistor Performance with Oxide Seeded High-kappa Gate Dielectrics on Wafer-Scale Epitaxial Graphene. *Nano Lett.* **2011**, *11*, 3601−3607.
(24) Bidmeshkipour, S.; Vorobiev, A.; Andersson, M. A.; Kompany, A.; Stake, J. Effect of ferroelectric substrate on carrier mobility in graphene field-effect transistors. *Appl. Phys. Lett.* **2015**, *107*, 173106.
(25) Chen, F.; Xia, J. L.; Ferry, D. K.; Tao, N. J. Dielectric Screening Enhanced Performance in Graphene FET. *Nano Lett.* **2009**, *9*, 2571−2574.
(26) Li, X. S.; Cai, W. W.; An, J. H.; Kim, S.; Nah, J.; Yang, D. X.; Piner, R.; Velamakanni, A.; Jung, I.; Tutuc, E.; Banerjee, S. K.; Colombo, L.; Ruoff, R. S. Large-Area Synthesis of High-Quality and Uniform Graphene Films on Copper Foils. *Science* **2009**, *324*, 1312−1314.
(27) Rahimi, S.; Tao, L.; Chowdhury, S. F.; Park, S.; Jouvray, A.; Buttress, S.; Rupesinghe, N.; Teo, K.; Akinwande, D. Toward 300 mm Wafer-Scalable High-Performance Polycrystalline Chemical Vapor Deposited Graphene Transistors. *ACS Nano* **2014**, *8*, 10471−10479.
(28) Ho, V. X.; Wang, Y.; Cooney, M. P.; Vinh, N. Q. Graphene-Ta_2O_5 Heterostructure Enabled High Performance, Deep-Ultraviolet to Mid-Infrared Photodetection. *Nanoscale* **2021**, *13*, 10526−10535.
(29) Wang, Y. F.; Ho, V. X.; Pradhan, P.; Cooney, M. P.; Vinh, N. Q. Interfacial Photogating Effect for Hybrid Graphene-Based Photodetectors. *ACS Appl. Nano Mater.* **2021**, *4*, 8539−8545.
(30) Leotin, J. Far infrared photoconductivity studies in silicon blocked impurity band structures. *Infrared Phys. Technol.* **1999**, *40*, 153−160.
(31) Seguini, G.; Schamm-Chardon, S.; Pellegrino, P.; Perego, M. The energy band alignment of Si nanocrystals in SiO2. *Appl. Phys. Lett.* **2011**, *99*, 082107.
(32) Novikov, A. Experimental measurement of work function in doped silicon surfaces. *Solid State Electron.* **2010**, *54*, 8−13.
(33) Hwang, T. J.; Rogers, S. H.; Li, B. Z. Work Function Measurement of Tungsten Polycide Gate Structures. *J. Electron. Mater.* **1983**, *12*, 667−679.
(34) Yan, R.; Zhang, Q.; Li, W.; Calizo, I.; Shen, T.; Richter, C. A.; Hight-Walker, A. R.; Liang, X.; Seabaugh, A.; Jena, D.; et al. Determination of graphene work function and graphene-insulator-semiconductor band alignment by internal photoemission spectroscopy. *Appl. Phys. Lett.* **2012**, *101*, 022105.
(35) Wang, Y.; Ho, V. X.; Henschel, Z. N.; Cooney, M. P.; Vinh, N. Q. Effect of High-K Dielectric Layer on 1/f Noise Behavior in Graphene Field-Effect Transistors. *ACS Appl. Nano Mater.* **2021**, *4*, 3647−3653.
(36) Liao, K. S.; Li, N.; Wang, C.; Li, L.; Jing, Y. L.; Wen, J.; Li, M. Y.; Wang, H.; Zhou, X. H.; Li, Z. F.; Lu, W. Extended mode in blocked impurity band detectors for terahertz radiation detection. *Appl. Phys. Lett.* **2014**, *105*, 143501.
(37) Huffman, J. E.; Crouse, A. G.; Halleck, B. L.; Downes, T. V.; Herter, T. L. Si-Sb Blocked Impurity Band Detectors for Infrared Astronomy. *J. Appl. Phys.* **1992**, *72*, 273−275.
(38) Geist, J. Infrared-Absorption Cross-Section of Arsenic in Silicon in the Impurity Band Region of Concentration. *Appl. Opt.* **1989**, *28*, 1193−1199.
(39) Bandaru, J.; Beeman, J. W.; Haller, E. E. Far-infrared absorption in Sb-doped Ge epilayers near the metal-insulator transition. *Appl. Phys. Lett.* **2002**, *80*, 3536−3538.
(40) Beeman, J. W.; Goyal, S.; Reichertz, L. A.; Haller, E. E. Ion-implanted Ge: B far-infrared blocked-impurity-band detectors. *Infrared Phys. Technol.* **2007**, *51*, 60−65.
(41) Ramdas, A. K.; Rodriguez, S. Spectroscopy of the Solid-State Analogs of the Hydrogen-Atom - Donors and Acceptors in Semiconductors. *Rep. Prog. Phys.* **1981**, *44*, 1297−1387.
(42) Rumyantsev, V. V.; Morozov, S. V.; Kudryavtsev, K. E.; Gavrilenko, V. I.; Kozlov, D. V. Features of impurity-photoconductivity relaxation in boron-doped silicon. *Semiconductors* **2012**, *46*, 1387−1391.
(43) Guo, X. T.; Wang, W. H.; Nan, H. Y.; Yu, Y. F.; Jiang, J.; Zhao, W. W.; Li, J. H.; Zafar, Z.; Xiang, N.; Ni, Z. H.; Hu, W. D.; You, Y. M.; Ni, Z. H. High-performance graphene photodetector using interfacial gating. *Optica* **2016**, *3*, 1066−1070.
(44) Luo, F.; Zhu, M. J.; tan, Y.; Sun, H. H.; Luo, W.; Peng, G.; Zhu, Z. H.; Zhang, X. A.; Qin, S. Q. High responsivity graphene photodetectors from visible to near-infrared by photogating effect. *AIP Adv.* **2018**, *8*, 115106.
(45) Shimatani, M.; Ogawa, S.; Fujisawa, D.; Okuda, S.; Kanai, Y.; Ono, T.; Matsumoto, K. Giant Dirac point shift of graphene phototransistors by doped silicon substrate current. *AIP Adv.* **2016**, *6*, 035113.
(46) Ogawa, S.; Shimatani, M.; Fukushima, S.; Okuda, S.; Kanai, Y.; Ono, T.; Matsumoto, K. Broadband photoresponse of graphene photodetector from visible to long-wavelength infrared wavelengths. *Opt. Eng.* **2019**, *58*, 057106.
(47) Lee, C. J.; Park, H.; Kang, J.; Lee, J.; Choi, M.; Park, H. Extraction of intrinsic field-effect mobility of graphene considering effects of gate-bias-induced contact modulation. *J. Appl. Phys.* **2020**, *127*, 185105.
(48) Christensen, C.; Reus, R.; Bouwstra, S. Tantalum oxide thin films as protective coatings for sensors. *J. Micromech. Microeng.* **1999**, *9*, 113−118.
(49) Demiryont, H.; Sites, J. R.; Geib, K. Effects of Oxygen-Content on the Optical-Properties of Tantalum Oxide-Films Deposited by Ion-Beam Sputtering. *Appl. Opt.* **1985**, *24*, 490−495.
(50) Yu, X. C.; Dong, Z. G.; Liu, Y. P.; Liu, T.; Tao, J.; Zeng, Y. Q.; Yang, J. K. W.; Wang, Q. J. A high performance, visible to mid-infrared photodetector based on graphene nanoribbons passivated with HfO2. *Nanoscale* **2016**, *8*, 327−332.
(51) Song, S. J.; Park, T.; Yoon, K. J.; Yoon, J. H.; Kwon, D. E.; Noh, W.; Lansalot-Matras, C.; Gatineau, S.; Lee, H. K.; Gautam, S.; Cho, D. Y.; Lee, S. W.; Hwang, C. S. Comparison of the Atomic Layer Deposition of Tantalum Oxide Thin Films Using Ta((NBu)-But)(NEt2)(3), Ta(NtBu)(NEt2)(2)Cp, and H2O. *ACS Appl. Mater. Interfaces* **2017**, *9*, 537−547.

https://doi.org/10.1021/acsanm.2c02011
ACS Appl. Nano Mater. 2022, 5, 12477−12486

(52) Morikawa, T.; Saeki, S.; Suzuki, T.; Kajino, T.; Motohiro, T. Dual functional modification by N doping of Ta2O5: p-type conduction in visible-light-activated N-doped Ta2O5. *Appl. Phys. Lett.* **2010**, *96*, 142111.
(53) Chennakesavulu, K.; Reddy, G. R. Synthesis and characterization of carbon microtube/tantalum oxide composites and their photocatalytic activity under visible irradiation. *RSC Adv.* **2015**, *5*, 56391−56400.
(54) Zhang, J. Y.; Lim, B.; Boyd, I. W. Thin tantalum pentoxide films deposited by photo-induced CVD. *Thin Solid Films* **1998**, *336*, 340−343.
(55) Kim, S.; Nah, J.; Jo, I.; Shahrjerdi, D.; Colombo, L.; Yao, Z.; Tutuc, E.; Banerjee, S. K. Realization of a high mobility dual-gated graphene field-effect transistor with Al2O3 dielectric. *Appl. Phys. Lett.* **2009**, *94*, 062107.
(56) Chen, K.; Wan, X.; Liu, D. Q.; Kang, Z. W.; Xie, W. G.; Chen, J.; Miao, Q.; Xu, J. B. Quantitative determination of scattering mechanism in large-area graphene on conventional and SAM-functionalized substrates at room temperature. *Nanoscale* **2013**, *5*, 5784−5793.
(57) Wang, N.; Ma, Z. H.; Ding, C.; Jia, H. Z.; Sui, G. R.; Gao, X. M. Characteristics of Dual-Gate Graphene Thermoelectric Devices Based on Voltage Regulation. *Energy Technol.* **2020**, *8*, 1901466.
(58) Baklanov, M.; Green, M.; Maex, K. *Dielectric Films for Advanced Microelectronics*; John Wiley & Sons, Ltd, 2007.
(59) Masetti, G.; Severi, M.; Solmi, S. Modeling of Carrier Mobility against Carrier Concentration in Arsenic-Doped, Phosphorus-Doped, and Boron-Doped Silicon. *IEEE Trans. Electron Devices* **1983**, *30*, 764−769.
(60) Basu, S.; Lee, B. J.; Zhang, Z. M. Infrared Radiative Properties of Heavily Doped Silicon at Room Temperature. *J. Heat. Transfer* **2010**, *132*, 023301.
(61) Van Overstraeten, R. J.; Mertens, R. P. Heavy Doping Effects in Silicon. *Solid State Electron.* **1987**, *30*, 1077−1087.
(62) Selberherr, S. *Analysis and Simulation of Semiconductor Devices*; Springer-Verlag/Wien, 1984.
(63) Mertens, R. P.; Van Overstraeten, R. J.; De Man, H. J. Advances in Electronics and Electron Physics. *Heavy Doping Effects in Silicon*; Academic Press, Inc, 1981; Vol. *55*.
(64) Kufer, D.; Konstantatos, G. Photo-FETs: Phototransistors Enabled by 2D and OD Nanomaterials. *ACS Photonics* **2016**, *3*, 2197−2210.
(65) Kayyalha, M.; Chen, Y. P. Observation of reduced 1/f noise in graphene field effect transistors on boron nitride substrates. *Appl. Phys. Lett.* **2015**, *107*, 113101.
(66) Liu, C. H.; Chang, Y. C.; Norris, T. B.; Zhong, Z. H. Graphene photodetectors with ultra-broadband and high responsivity at room temperature. *Nat. Nanotechnol.* **2014**, *9*, 273−278.
(67) Guo, W. H.; Xu, S. G.; Wu, Z. F.; Wang, N.; Loy, M. M. T.; Du, S. W. Oxygen-Assisted Charge Transfer Between ZnO Quantum Dots and Graphene. *Small* **2013**, *9*, 3031−3036.
(68) Sun, Z. H.; Liu, Z. K.; Li, J. H.; Tai, G. A.; Lau, S. P.; Yan, F. Infrared Photodetectors Based on CVD-Grown Graphene and PbS Quantum Dots with Ultrahigh Responsivity. *Adv. Mater.* **2012**, *24*, 5878−5883.
(69) Chen, S. Y.; Lu, Y. Y.; Shih, F. Y.; Ho, P. H.; Chen, Y. F.; Chen, C. W.; Chen, Y. T.; Wang, W. H. Biologically inspired graphene-chlorophyll phototransistors with high gain. *Carbon* **2013**, *63*, 23−29.
(70) Liu, Y. P.; Xia, Q. L.; He, J.; Liu, Z. W. Direct Observation of High Photoresponsivity in Pure Graphene Photodetectors. *Nanoscale Res. Lett.* **2017**, *12*, 93.
(71) Green, M. A. Self-consistent optical parameters of intrinsic silicon at 300 K including temperature coefficients. *Sol. Energy Mater. Sol. Cells* **2008**, *92*, 1305−1310.

NOTE ADDED AFTER ASAP PUBLICATION

This paper was published ASAP on August 15, 2022, with errors in Figure S6. The corrected version was reposted on August 19, 2022.

https://doi.org/10.1021/acsanm.2c02011
ACS Appl. Nano Mater. 2022, 5, 12477−12486

SUPPORTING INFORMATION

Shallow Impurity States in Doped Silicon Substrates Enabling High Responsivity for Graphene Mid-Infrared Photodetectors

Vinh X. Ho,[1] Yifei Wang,[1] Leslie Howe,[1], Michael P. Cooney,[2] and Nguyen Q. Vinh[1]*

[1] Department of Physics and Center for Soft Matter and Biological Physics, Virginia Tech, Blacksburg, VA 24061, USA

[2] NASA Langley Research Center, Hampton, Virginia 23681, USA

* Corresponding author: vinh@vt.edu; phone: 1-540-231-3158

1. Device fabrication

We have fabricated graphene field-effect transistor (Gr-FET) photodetectors on both p-type boron-doped silicon (Si:B) and n-type phosphorus-doped silicon (Si:P) wafers with different doping concentrations of 3.0×10^{15}, 4.8×10^{18} and 4.6×10^{19} cm^{-3}. First, an 80-nm dry thermal oxide layer was grown on these Si wafers at 1100 ^{o}C. Drain, source, and back-gate contacts (5 nm Cr and 100 nm Au) were fabricated by photolithography, electron-beam (e-beam) evaporation, and metal lift-off processes. The Si/SiO_2 wafers with metal contacts were cleaned by argon plasma in 4 minutes to minimize photoresist residue after the lift-off process. Graphene on copper (Cu) foil was grown by chemical vapor deposition (CVD) method from Graphenea Inc. Poly(methyl methacrylate) (PMMA, MicroChem 495 PMMA A4 - (4% in Anisole) - 495,000 molecular weight) solution was spin-coated on the graphene/Cu foil at 1700 rpm for 45 seconds and dried in vacuum in 2 hours. A 0.3 M ammonium persulfate ($(NH_4)_2S_2O_8$, Sigma−Aldrich, ≥ 98%) aqueous solution was employed to etch the Cu foil at 30 ^{o}C in 1.5

hours. The graphene sheet was rinsed in deionized water two times in 5 minutes each time to remove residual Cu etchant. After that, the graphene sheet was transferred to the well-prepared Si/SiO_2 substrate with metal contacts. The sample was put in a vacuum chamber overnight to promote good adhesion. Hereafter, the sample was heated by a hot plate at 135 ºC in 20 minutes to enable the flattening of the graphene film and produce stronger adhesion. After that, PMMA was cleaned by putting them in acetone in 1 hour at 50 ºC, followed by IPA in 30 minutes at room temperature. The photolithography and argon-plasma etching were conducted to define the graphene channel with the distance, *L*, between drain and source of 6 µm, and the width, *W*, of 15 µm. Next, a 2-nm Ta_2O_5 seed layer was grown by an e-beam evaporation system (PRO line PVD 250, Kurt J. Lesker) with a rate of 0.1 Å/s. A 50-nm Ta_2O_5 film was then grown in an atomic layer deposition (ALD) system (Savannah S100 ALD, Cambridge Nanotech Inc.) at 300 ºC. Precursors of pentakis(dimethylamino)tantalum (V) and water were sequentially exposed with nitrogen gas. The deposition rate is ~0.53 Å/cycle. Finally, the photolithography and dry-etching using SF_6 gas were employed to re-define metal contacts.[1-6] A schematic diagram showing fabrication steps of the Gr-FET photodetector is illustrated in Figure S1.

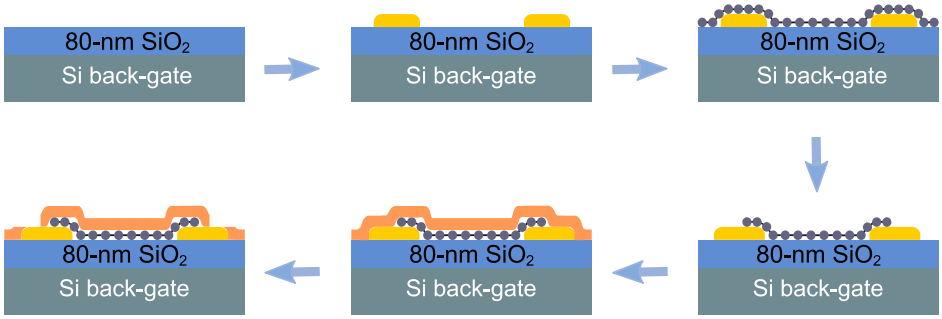

Figure S1. A schematic diagram showing fabrication steps of G-FET photodetectors.

2. Raman spectrum

The quality of a single-layer graphene on a Si/SiO_2 substrate was confirmed by Raman spectroscopy. The measurements were carried out by using a WITec UHTS 300 micro-Raman spectrometer under an excitation of a 663.1 nm laser. Two peaks at ~ 1585 cm^{-1} (G band) and ~ 2690 cm^{-1} (2D band) have been observed (Figure S2). The 2D band has only a single component with the FWHM of 33 cm^{-1}. The intensity ratio of the 2D band to the G band, I_{2D}/I_G, is 6.78, confirming a high quality of the single-layer graphene.[7] In addition, the D band at ~ 1350 cm^{-1} representing graphene defects from the transferring process of graphene was not observed.[8] A high-quality of the single-layer graphene has been obtained after the transferring process.

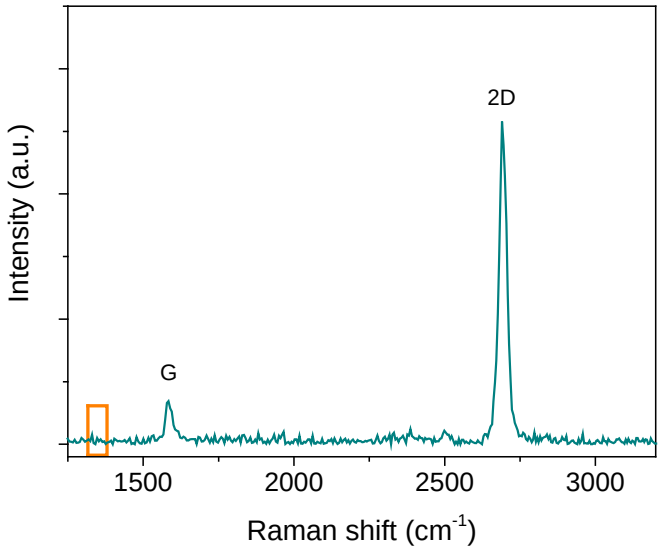

Figure S2. The Raman spectrum of a CVD single-layer graphene after transferring on a Si/SiO_2 wafer.

3. Absorption spectrum in mid-IR of Si:P materials

The absorption of shallow acceptors and donors in silicon has been observed by a Fourier-transform infrared (FTIR) spectrometer with a resolution of 0.15 cm^{-1}. Absorption spectra of a Si:P sample with a doping concentration of 3.0×10^{15} cm^{-3} at 10 K and 80 K are provided in Figure S3. A series of absorption lines corresponding to Lyman transitions from the ground state, $1s(A_1)$, to excited p states, np_0, $np_\pm$ (i.e., n = 2, 3, 4…), has observed in the range of 20 – 52 μm.

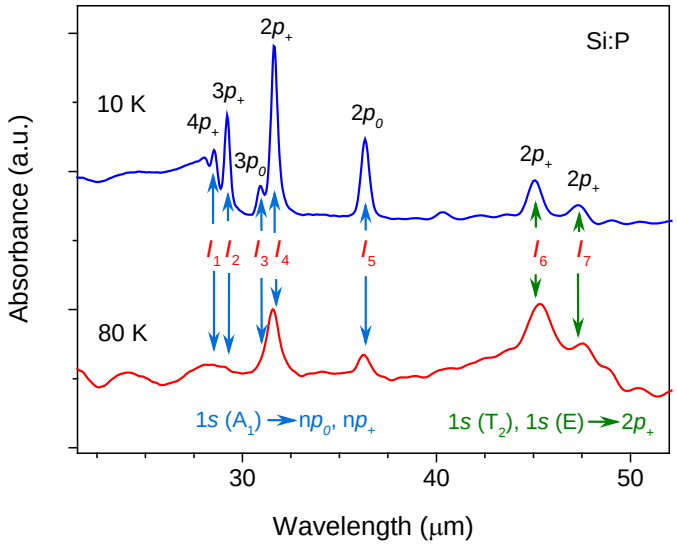

Figure S3. Fourier-transform infrared (FTIR) spectra of Si:P at 10 K and 80 K.

4. Optical and electrical set-ups

The photoresponse characteristics of Gr-FET detectors with and without light illumination at room temperature have been characterized by two electronical systems (Figure S4). A Keithley 2450 was used to set the drain-source bias, V_{DS}, and collect the drain current, I_D, while the other Keithley 2450 was employed to control the back-gate bias, V_{BG}, from -30 V to 30 V. A lock-in amplifier has been employed to collect photocurrent under a low illumination power of femto-watt.

a)

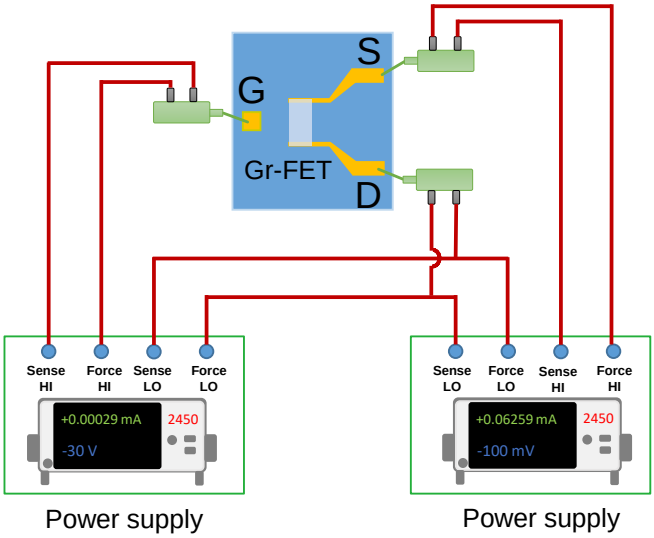

b)

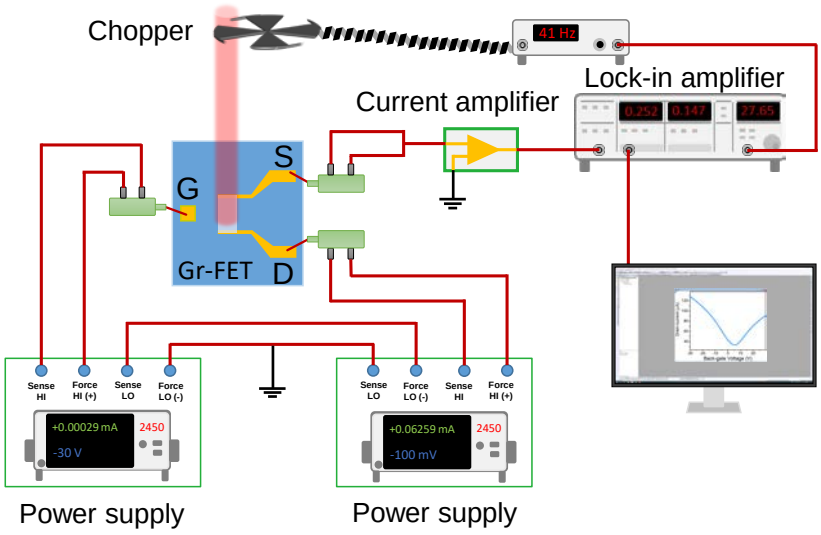

Figure S4. Two electrical setups have been used to collect photocurrent. The setups include source-meter units (Keithley 2450), a lock-in amplifier, and an oscilloscope.

Several laser sources with wavelengths of 532 nm, 4.55 µm, 8.5 µm, and 10.6 µm and an Edmund Tungsten lamp visible to near-IR source have been used to characterize the photoresponse of the devices (Figure S5). Using narrow band-pass filters, we have extracted light with a narrow bandwidth from the lamp. The continuous laser beams were chopped by an optical chopper or acousto-optic modulator (AOM). The rise time of pulses is 20 ns. A half-wave plate and polarizing beam-splitter, and several Thorlabs neutral density filters were used to control illumination power. A beam expander including two lenses with f_1 = 25 mm and f_2 = 500 mm was used to increasing the diameter of a laser beam. Devices were put in a black anodized aluminum chamber to prevent random light from ambient. A diaphragm with a 5 mm diameter on the cap of a black anodized aluminum box was employed to select a homogeneous part of the expanded beam.

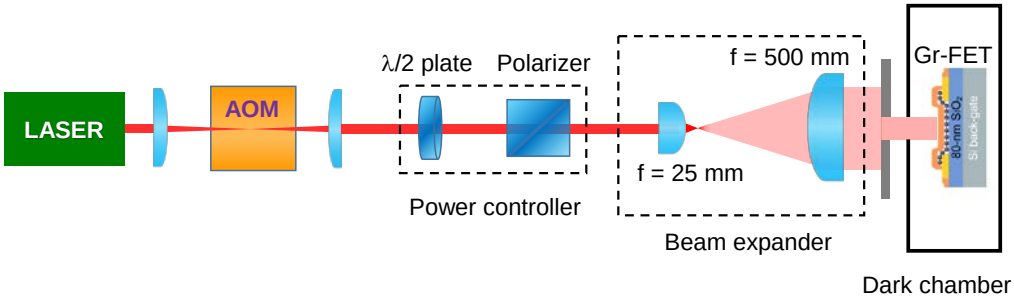

Figure S5. Optical set-up has been used to characterize photoresponse of Gr-FET photodetectors. Devices were put in a black anodized aluminum chamber to prevent random light from ambient.

5. Photoresponse of graphene photodetectors in the visible region

To elucidate the effect of doping concentration in Si substrate on the performance of graphene photodetectors, we have systematically investigated the photoresponse of the Gr-FET photodetectors on both p- and n-type silicon wafers with different doping concentrations under the visible and mid-IR illumination. All measurements have been performed at room temperature.

The photoresponse of Gr-FET photodetectors on a p-type Si substrate with a light doping concentration ($n = 3 \times 10^{15}$ cm^{-3}) in the visible region has been characterized under different driven voltages. The back-gate bias, V_{BG}, is varied from -30 V to 30 V, while the drain-to-source bias, V_{DS}, is fixed at 0.1 V. The current-voltage ($I - V$) characteristic curves under dark and light illumination of the 532 nm laser were measured at room temperature (Figure 6a). The $I - V$ characteristic curves shift toward the positive of the back-gate bias. In other words, the charge neutrality point (CNP) voltage, V_{Dirac}, of the $I - V$ characteristic curves moves toward the positive of the back-gate voltage when the illumination power is varied from 0.11 nW to 1.09 nW. The drain current, I_D, increases with $V_{BG} < V_{Dirac}$ and decreases for $V_{BG} > V_{Dirac}$ (Figure 6b).

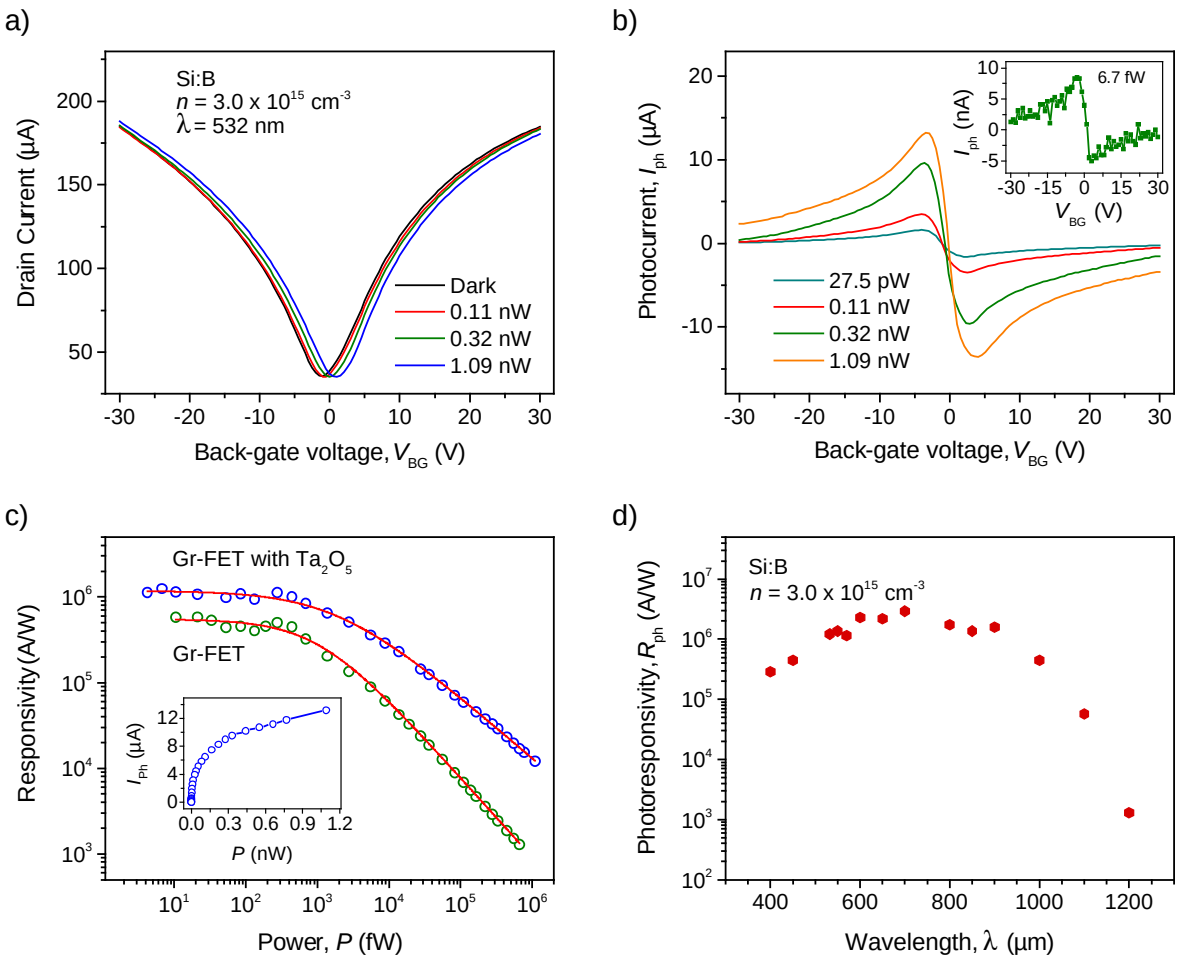

Figure S6. Photoresponse of an Gr-FET on a lightly-doped p-type Si substrate (n = 3×10^{15} cm^{-3}) has been characterized under λ = 532 nm and V_{DS} = 0.1 V. (**a**) Current – Voltage (I – V) characteristics of the Gr-FET without an ALD Ta_2O_5 capping layer have been measured under different illumination powers. (**b**) Photocurrent curves of the Gr-FET as a function of back-gate voltage have been collected under different illumination powers. The inset shows photocurrent under an illumination power of 6.7 fW. (**c**) The photoresponsivity of the Gr-FETs with and without an ALD Ta_2O_5 capping layer. The inset shows power dependence of photocurrent at V_{BG} = 3.5 V. (**d**) Photoresponsivity of the Gr-FET with an ALD Ta_2O_5 capping layer from 400 to 1200 nm under V_{DS} = 0.1 V.

We have performed the power dependence of photocurrent and calculated the photoresponsivity. The photocurrent is calculated by $I_{ph} = I_{illumination} - I_{dark}$, where $I_{illumination}$ and I_{dark} are the current values under illumination and dark conditions, respectively. The photocurrent under different excitation power is presented as a function of the back-gate voltage and reaches a maximum value at V_{BG} = 3.5 V (Figure

S6b). The photocurrent at V_{BG} = 3.5 V under different excitation powers of the 532 nm laser is presented in the inset of Figure S6c. The photocurrent increases linearly under a weak illumination power from 7 fW to 1.5 pW and rises slowly under high radiation power. The detectors are extremely sensitive to light. A net photocurrent value of ~8.5 nA has been observed under an illumination power ~ 6.7 fW (Figure S6b, inset).

To explore the performance of the detectors the photoresponsivity, R_{ph}, of the devices has been determined, $R_{ph} = I_{ph}/P$, where P is power on the device and I_{ph} is photocurrent. The photoresponsivity as a function of illumination power is plotted in the inset of Figure S6c. The linear power dependence of photocurrent was detected under low illumination power, showing a constant of the photoresponsivity. The detectors show a high photoresponsivity of ~1.2×10^6 A/W under λ = 532 nm for almost three orders of magnitude of illumination power from fW to pW scale, allowing for weak light detection. It is because electrons and holes generated from the photoabsorption process are well separated under low illumination power region; thus, a higher number of photons will produce a higher electrical current. However, under a high illumination power, a higher number of electron-hole pairs is generated. Some holes recombine with electrons, and thus, these holes do not contribute to the photocurrent. Thus, the growth of the photocurrent with increasing illumination power has been slow down, and the photoresponsivity is reduced at high illumination power. Figure 6Sd presents the photoresponsivity as a function of wavelengths from 400 nm to 1200 nm with the highest photoresponsivity of ~ 3.0×10^6 A/W at 700 nm under V_{DS} = 0.1 V.

6. Response time of Gr-FET photodetectors on Si:B substrate in the visible region

The rise time consists of two components, including a fast, τ_{1R}, and a slow, τ_{2R}, component that are obtained by an exponential function, $I_{ph} = I_0 - A\exp\left(-t/\tau_{1R}\right) - B\exp\left(-t/\tau_{2R}\right)$. The fast rise time, τ_{1R} ~ 20 ns, accounts for 70% of the rise time, which corresponds to the carrier transit time in the graphene channel. The carrier mobility, μ, was estimated at ~ 10538 $cm^2/(V.s)$. The carrier transit time between the source and drain can be calculated by, $\tau_{1R} = (L/V_{\text{drift}}) = L^2\mu^{-1}V_{DS}^{-1}$. It is ~ 0.34 ns instead of 20 ns. The difference is due to the rise time of the 532 nm laser pulse of 20 ns, much slower than the carrier transit time. The slow rise time, τ_{2R} ~ 360 ns, represents the average diffusion time of photogenerated carriers to the potential well at the Si/SiO_2 interface. The fall time of the photodetector can be analyzed with an exponential decay function, $I_{ph} = C\exp\left(-t/\tau_{1F}\right) + D\exp\left(-t/\tau_{2F}\right)$. The fast fall time constant, τ_{1F}, ~ 500 ns. This value is similar with the slow rise time, τ_{2R}, which can be originated from the average diffusion time of photogenerated carriers out of the potential well at the Si/SiO_2 interface after the light pulse is turned off. The slow fall time constant, τ_{2F} ~ 42 μs, is contributed by charged centers with a long lifetime in SiO_2 near the Si/SiO_2 interface.

7. Response time of Gr-FET photodetectors on Si:B substrate in the mid-IR region

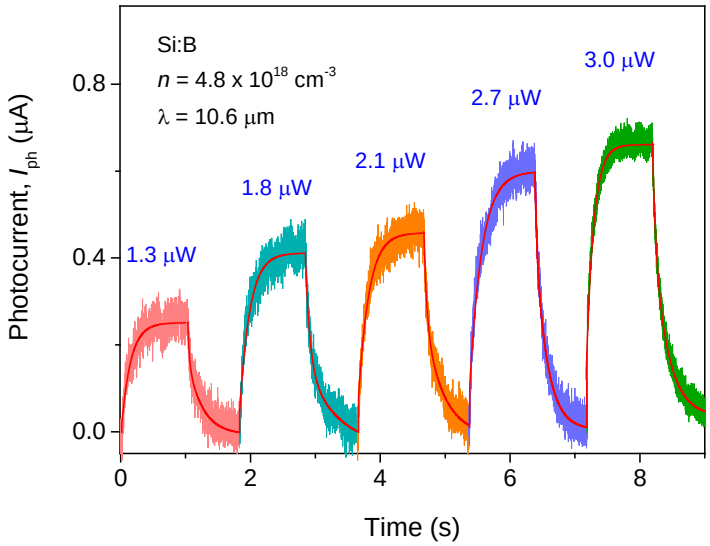

Figure S7. Response time of Gr-FETs on a Si:B substrate (n = 4.8 × 10^{18} cm^{-3}) with an ALD Ta_2O_5 capping layer under the mid-IR illumination from a 10.6 μm laser with V_{DS} = 0.1 V at room temperature.

8. Photocurrent of Gr-FET photodetectors on Si:B and Si:P substrates in the mid-IR region

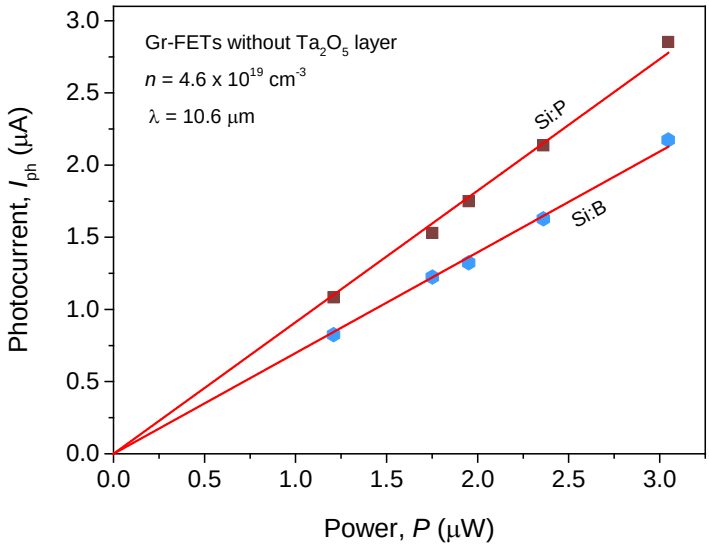

Figure S8. Photocurrent of Gr-FETs on highly-doped Si:B and Si:P substrates without an ALD Ta_2O_5 capping layer under the 10.6-μm illumination with V_{DS} = 0.1 V at room temperature.

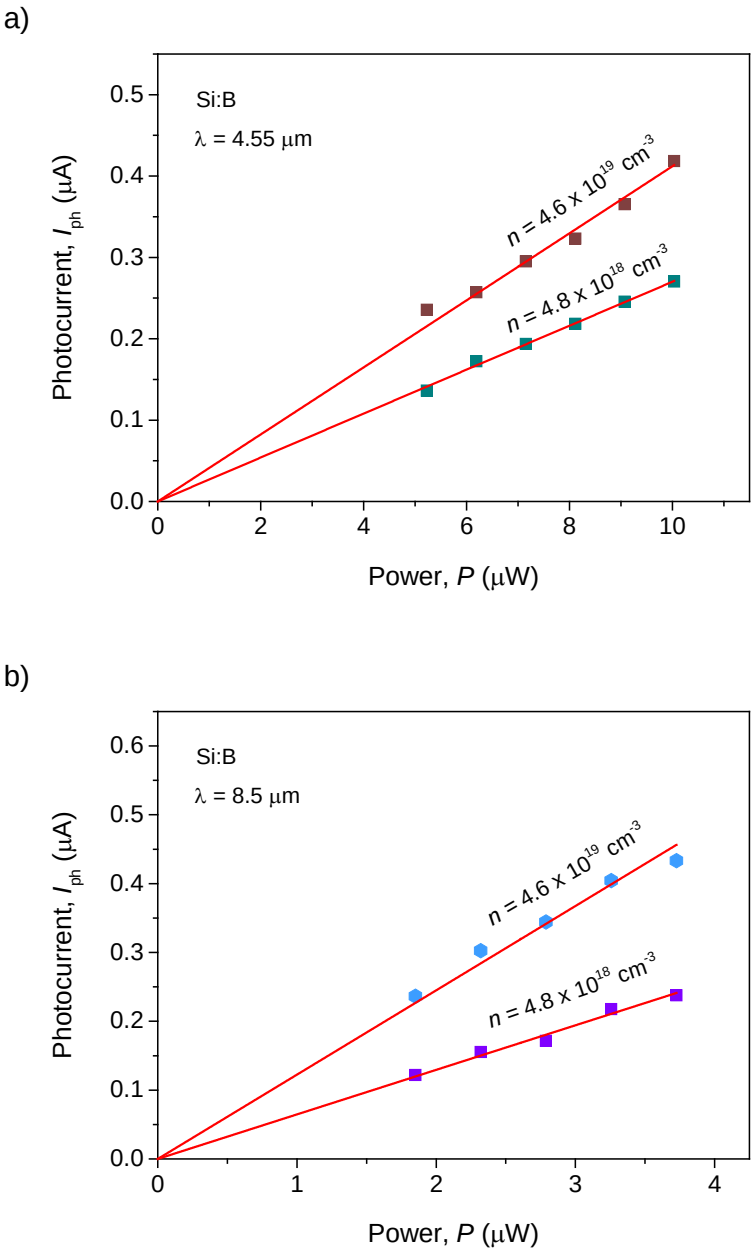

Figure S9. Photocurrent of Gr-FETs on highly-doped Si:B substrates with an ALD Ta_2O_5 capping layer under the mid-IR illumination with the wavelength of (**a**) 4.55 μm and (**b**) 8.5 μm and V_{DS} = 0.1 V at room temperature.

9. Photoresponsivity of Gr-FET photodetectors on Si:P substrate with and without an ALD Ta_2O_5 capping layer in the mid-IR region

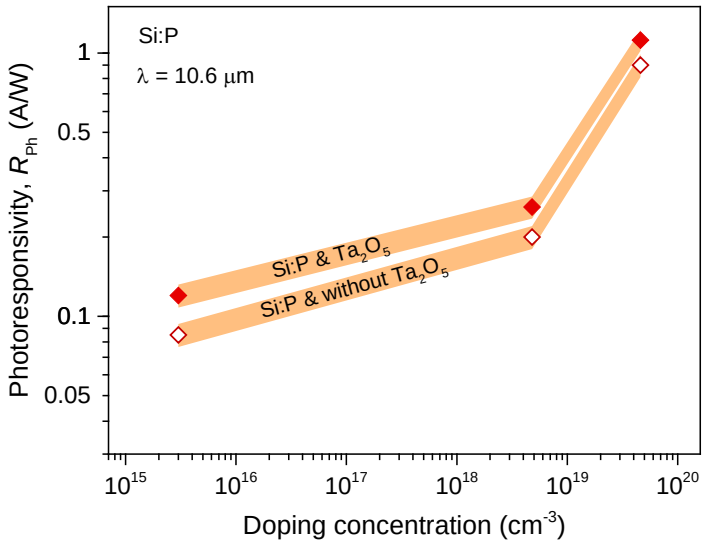

Figure S10. Photoresponsivity of Gr-FETs on a Si:P substrate (n = 4.6 × 10^{19} cm^{-3}) with and without an ALD Ta_2O_5 capping layer at 10.6 μm.

10. Noise characterization

To characterize the 1/f noise, a Keithley 2450 source-meter unit was used to vary the back-gate voltage, V_{BG}, while the other was employed to set a drain-source voltage. A FEMTO DLPCA-200 low-noise current amplifier was used to amplify the drain current. A 100 kHz FFT spectrum analyzer (Stanford Research 770 – SR770) was utilized to characterize the noise behavior of Gr-FET photodetectors without illumination.

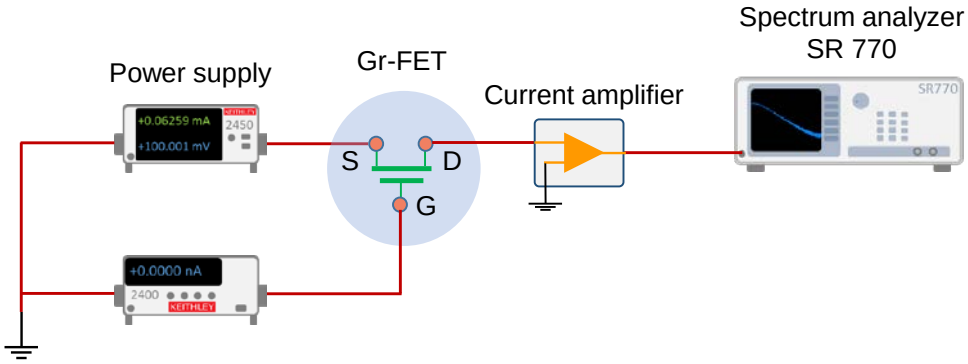

Figure S11. A schematic for 1/f noise measurements.

The noise equivalent power (NEP) and the specific detectivity (D^*) are important parameters of a photodetector, which can be calculated by investigating the power spectral density of $1/f$ noise, shot noise, and thermal noise of Gr-FET photodetectors.

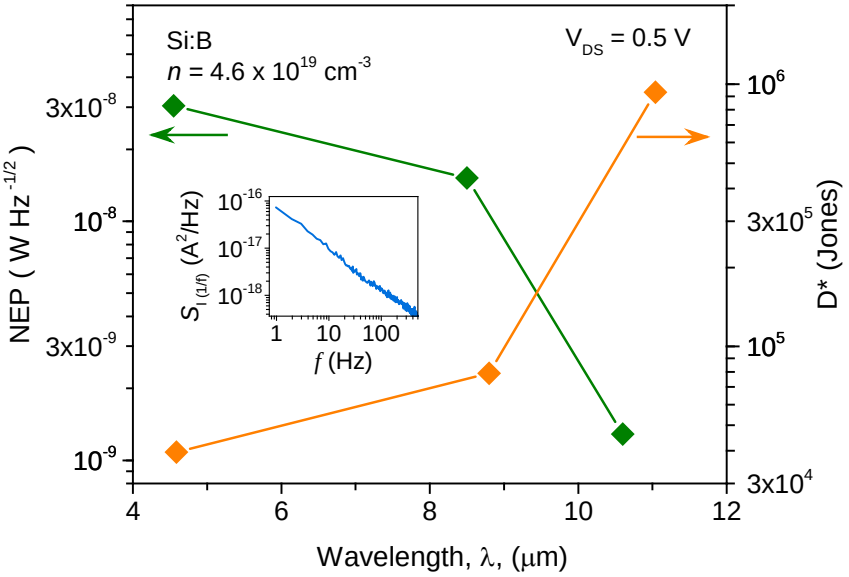

Figure S12. The noise equivalent power (NEP) and the specific detectivity (D^*) of Gr-FETs on Si:B substrates with a Ta_2O_5 cap layer under V_{DS} = 0.5 V at room temperature.

The spectral density (S_I) of the $1/f$ noise (or flicker noise) in the dark condition can be expressed as.[9]

$$S_I(1/f) = \frac{AI_{dark}^2}{f^\beta}, \quad \text{(S1)}$$

where A is the noise amplitude, and β is close to 1. The spectra are dominated by the $1/f$ noise up to 1 kHz. The spectral density of the $1/f$ noise is 5.4 × 10^{-18} A^2/Hz and 5.7 × 10^{-17} A^2/Hz at the drain-to-source voltage, V_{DS}, of 0.1 V and 0.5V, respectively.

The spectral density of shot noise is given by:

$$S_I(\text{shot}) = \sqrt{2qI_{dark}}, \quad \text{(S2)}$$

where q is the elemental charge, and I_{dark} is the dark current of the device. The calculated spectral density of shot noise is ~ 1.1 × 10^{-23} A^2/Hz and 5.8 × 10^{-23} A^2/Hz at the drain-to-source voltage, V_{DS}, of 0.1 V and 0.5V, respectively.

The spectral density of thermal noise is estimated by the Nyquist's equation:

$$S_I(\text{thermal}) = \sqrt{4k_BT/R} \quad \text{(S3)}$$

where k_B is the Boltzmann's constant, T is the temperature, and R is the differential resistance of the device in the dark. The thermal noise at room temperature is estimated ~ 1.61 × 10^{-25} A^2/Hz and 1.59 × 10^{-25} A^2/Hz at the drain-to-source voltage, V_{DS}, of 0.1 V and 0.5V, respectively.

11. SEM images of the Gr-FET photodetectors with different sizes of cannels

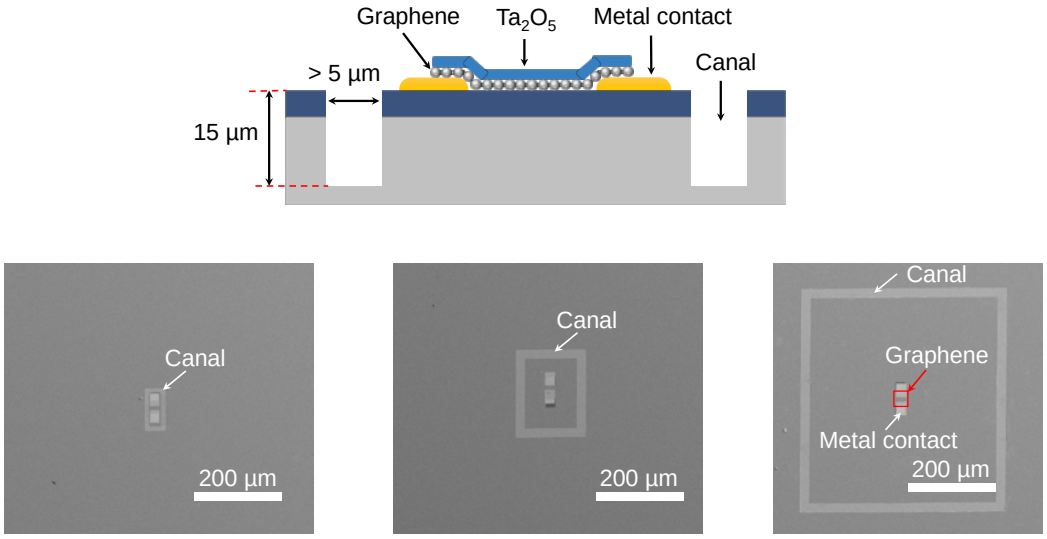

Figure S13. (**a**) A schematic for the cross-section of a Gr-FET photodetector with a canal around the device. (**b**) SEM images of Gr-FET photodetectors with different sizes of canal, and the distance from the graphene channel to the canal edge is 2, 50, and 200 µm.

References

(1) Ho, V. X.; Wang, Y.; Cooney, M. P.; Vinh, N. Q. Graphene-Ta_2O_5 Heterostructure Enabled High Performance, Deep-Ultraviolet to Mid-Infrared Photodetection. *Nanoscale* **2021,** *13*, 10526-10535.

(2) Wang, Y.; Ho, V. X.; Henschel, Z. N.; Cooney, M. P.; Vinh, N. Q. Effect of High-K Dielectric Layer on 1/f Noise Behavior in Graphene Field-Effect Transistors. *ACS Appl. Nano Mater.* **2021,** *4*, 3647-3653.

(3) Wang, Y. F.; Ho, V. X.; Pradhan, P.; Cooney, M. P.; Vinh, N. Q. Interfacial Photogating Effect for Hybrid Graphene-Based Photodetectors. *ACS Appl. Nano Mater.* **2021,** *4*, 8539-8545.

(4) Ho, V. X.; Wang, Y.; Cooney, M. P.; Vinh, N. Q. Graphene-Based Photodetector at Room Temperature. *Proc. SPIE* **2018,** *10729*, 1072907.

(5) Wang, Y.; Ho, V. X.; Pradhan, P.; Cooney, M. P.; Vinh, N. Q. Graphene-Germanium Quantum Dot Photodetector with High Sensitivity. *Proc. SPIE* **2019,** *11088*, 1108809.

(6) Wang, Y.; Ho, V. X.; Henschel, Z. N.; Pradhan, P.; Howe, L.; Cooney, M. P.; Vinh, N. Q. Graphene Photodetector Based on Interfacial Photogating Effect with High Sensitivity. *Proc. SPIE* **2020,** *11503*, 1150306.

(7) Malard, L. M.; Pimenta, M. A.; Dresselhaus, G.; Dresselhaus, M. S. Raman spectroscopy in graphene. *Phys. Rep.* **2009,** *473*, 51-87.

(8) Her, M.; Beams, R.; Novotny, L. Graphene transfer with reduced residue. *Phys. Lett. A* **2013,** *377*, 1455-1458.

(9) Kayyalha, M.; Chen, Y. P. Observation of reduced 1/f noise in graphene field effect transistors on boron nitride substrates. *Appl. Phys. Lett.* **2015,** *107*, 113101.